Simulation of observed temperature field below a building in Bologna, Italy

Published Version:
Focaccia, S., Barbaresi, A., Tinti, F. (2020). Simulation of observed temperature field below a building in Bologna, Italy. ENVIRONMENTAL GEOTECHNICS, 7(4), 295-305 [10.1680/jenge.17.00105].

Availability:
This version is available at: https://hdl.handle.net/11585/651692 since: 2024-07-18

Published:
DOI: http://doi.org/10.1680/jenge.17.00105

Simulation of observed temperature field below a building

Author 1

- Eng. PhD. Sara Focaccia
- SERENGEO srl, Bologna, Italy
- 0000-0002-1293-4914

Author 2

- Eng. PhD. Alberto Barbaresi
- Department of Agricultural Sciences, University of Bologna, Bologna, Italy
- 0000-0003-1341-984X

Author 3

- Eng. PhD. Francesco Tinti*
- Department of Civil, Chemical, Environmental and Materials Engineering, University of Bologna, Bologna, Italy
- 0000-0002-6750-9368

Paper submitted: 14/12/2017.

Paper revised: 15/05/2018.

*Corresponding Author: Francesco Tinti.

Department of Civil, Chemical, Environmental and Materials Engineering, University of Bologna, via Terracini 28, 40100 Bologna, Italy.

E-mail: francesco.tinti@unibo.it

Phone: +390512090477

Abstract

Urban settlements, whether single buildings or apartment blocks, influence near-surface ground temperatures. Heat transfer by buildings to the ground must therefore be considered when designing both vertical probes and energy geostructures in urban areas. However, assessment of ground temperature variability in urban areas is still uncommon for shallow geothermal energy purposes, the standard temperature gradient based on climatic conditions usually being employed during the design phase. Yet precise assessment of the heat transfer between buildings, infrastructures and the underground could improve the planning of geothermal systems.

This work presents a numerical simulation of a finite-element model of heat transfer to the underground due to both a single building and climate conditions with the aim of reproducing the temperature waves at each depth. An isolated building was chosen since it allowed exact quantification of its influence on the ground temperature without external interferences. For this purpose, different boundary and initial conditions were applied to the ground thermal model and results were compared with historical data recorded over several years. The idea proposed in the paper for a single building can be considered as the baseline for further ground temperature assessment of wider urban settlements.

Keywords

Ground temperature; Shallow geothermal energy; Finite-element modelling.

List of notation

T_g is the varying space-time underground temperature,

T_{me} is the average annual surface temperature,

$T_{building}$ is the temperature inside the building,

T_{cellar} is the temperature inside the cellar,

A_e is the annual surface wave amplitude,

t_{T0} is the time at minimum temperature,

α is the equivalent thermal diffusivity,

λ is the equivalent thermal conductivity,

ρ is the density,

C is the heat capacity,

$\rho \cdot C$ is the volumetric heat capacity.

1. Introduction

The subsurface temperature gradient, or geothermal gradient, depends mainly on endogenous geothermal heat flow (Cermak and Rybach, 1979). However, in shallow layers, its contribution is limited, and subsoil temperature follows climate seasonality, which is damped on account of ground thermal insulation that varies with geological and hydrogeological conditions (Kusuda and Achenbach, 1965). As a result, ground temperatures at very shallow depths change in space - vertically, because of climate wave dampening, and horizontally, due to the variation of geological and hydrogeological conditions - and time, following the ambient temperature wave (Baggs, 1985). It follows that at a certain depth and thickness, depending on local conditions, a ground layer, or so-called neutral zone, will exist where temperature variations in space and time become nil before geothermal heat flow resumes, with the resulting geothermal gradient (Pouloupatis et al., 2011).

Shallow layer ground temperature should also take into account urban ground warming (Ferguson and Woodbury, 2004). The replacement of natural soil and vegetation by artificial surfaces increases temperatures of the surrounding air and subsurface throughout the year on account of indirect solar heating of urban structures, building heat losses and land use change (Bornstein, 1968). At a district or city level, this phenomenon is called Urban Heat Island effect – UHI (Landsberg, 1981), and Subsurface Urban Heat Effect – SUHI, when referred to the thermal effect in the ground (Oke, 1982).

Heat loss from an individual building generates a bulb-shaped volume of subsurface temperatures that are higher compared to a non-urbanized context (Taniguchi et al., 2007) Several experimental studies have demonstrated that heat loss from buildings increases the subsurface temperature by several degrees (generally from 2 to 5 °C) and that this thermal impact is more persistent in the subsurface rather than in the air. Research on the topic has been performed in many part of the world, such as Japan (Huang et al., 2009; Taniguchi et al., 2007), Canada (Ferguson and Woodbury, 2007), Germany (Zhu et al., 2010; Menberg et al., 2013), Ireland (Allen et al., 2003), Turkey (Yalcin and Yetemen, 2009); United Kingdom (Headon et al., 2009); Finland (Arola and Korkka-Niemi, 2014) and Switzerland (Rivera et al., 2017). While calculating and estimating ground temperature distribution is useful in many fields of application, it becomes a key design element of:

- building basements, to minimize heat losses via the ground (e.g. Claesson and Hagentoft, 1991; Hagentoft and Claesson, 1991; Rees et al., 2000),
- cellars and underground spaces, to ensure appropriate goods storage conditions (e.g. Mazarron et al., 2012; Barbaresi et al., 2014),
- ground heat exchangers and energy geostructures, to assess shallow geothermal potential and simulate ground thermal behaviour during heat extraction and/or injection (e.g. Bandos et al., 2009; Kurevija and Vulin, 2010).

Dynamic simulators of flow, mass, and heat transfer in the underground are commonly used in the georesources and environmental fields (Pruess and Garcia, 2002; Zhao et al. 2005; Herbert and Chillingworth, 2013; Focaccia et al., 2016). In the geothermal sector, it is common practice to assign a constant ground temperature value to each subsoil layer as an input parameter. In shallow layers, this can be taken as the average ground temperature over the year, which is equivalent to the average ambient temperature (Al-Zyoud et al., 2014; Poulsen et al., 2015). In other case studies, the shallow layer temperature was experimentally measured in the field over a specific time period (Wu et al., 2010; Focaccia, 2013; Barla et al., 2018). In both cases, since shallow ground temperature is time dependent, the values assigned did not effectively represent the ground temperatures over the whole year. Numerical simulations of underground heat flow and mass transfer are not commonly designed to include the thermal effect of aboveground structures on ground temperature behaviour in shallow layers. However, identification of temperature variations in these shallow layers could improve the efficiency of exploitable geothermal energy through the use of energy piles.

The aim of this paper is to provide specific settings for dynamic simulations to include both time-related temperature variations and the thermal effects of buildings when designing energy geostructures where shallow layer temperatures may play a significant role. The simulation results were validated with a case study of a single building in a rural area that affected the ground temperature around it. The dynamic simulator settings were calibrated accordingly. Located in the countryside around Bologna, Italy, the detached house had already been used in several experimental and analytical investigations and been the object of a multiyear temperature and humidity measurement campaign. Measurements had been taken inside the building (Barbaresi et al., 2014), in the surrounding undisturbed ground at different depths (Tinti et al., 2014), inside the building cellar (Barbaresi et al., 2015) and beside and below the building at different depths (Tinti et al., 2015). Calculations and modeling were performed to improve cellar air temperature management (Benni et al., 2016) and estimate ground temperature evolution as a result of the building's presence (Tinti et al., 2017a).

2. Materials and methods

2.1. Choice of the numerical simulator

The numerical simulator *FEFLOW®* (Finite Element Flow simulator), commonly used in the shallow geothermal sector (Al-Khoury et al., 2005; Al-Khoury et al., 2006), was chosen for setting optimization. *FEFLOW®* is an integrated package including dynamic flow, heat and mass transportation simulation tools. It allows users to create as many layers as necessary and upload node by node database information for each layer (hydraulic properties, thermal properties, initial conditions of temperature and water level).

2.2. Model parameters: geology, hydrogeology and building dimensions.

The case study involved a two-storey building with an underground wine-ageing room in a rural area in the countryside of Bologna (Italy). The bearing is 32° north-east. The building's key features are reported in *Table 1*.

Table 1: *Key building features.*

	Two-storey building	**Wine-ageing room**
Width	9.8 m	5.6 m
Length	20.5 m (above ground) + 5.6 m (above cellar)	9.8 m
Height	7.3 m (borders), 8.4 m (centre)	2.6 m (underground)
Walls	25.0 cm thick masonry	25.0 cm thick masonry
Floor	30.0 cm hollow concrete slab	20.0 cm concrete slab
Ceiling	-	30.0 cm hollow concrete slab
Air conditioning	Heating and natural ventilation	Natural ventilation

A model PCE-FWS20 weather station located 100 m from the building collected the main weather data. The two-storey building is heated during the winter season, and there is no mechanical cooling during summer. A set of stand-alone temperature and humidity data loggers, model PCE-HT71, with a 0.1°C resolution, an accuracy of ±0.5°C and a 1 minute registration interval were chosen to collect data. Three were used to measure the internal ambient data (temperature and humidity) of the rooms of the two-storey building (Barbaresi et al., 2014). Seventeen data loggers were subsequently placed inside the exclusively naturally ventilated wine cellar (Barbaresi et al., 2015).

Subsoil temperature distribution in the intervention area had already been thoroughly analysed. Four monitoring boreholes, each with three data loggers, with integrated temperature sensors, placed at different depths, were drilled at designated positions with respect to the building. Boreholes I and II are vertical and are both equipped with three data loggers at depths of 2, 4 and 6 m (Numbered 1 to 6, Tinti et al., 2014). Borehole III, with a total length of 17 m, is inclined (10° from horizontal plane) and has 3 data loggers at depths of 1.8, 2.6 and 3.7 m, 2 of them (the deepest ones) being located below the building and beside the cellar (Numbered 7, 8 and 9, Tinti et al., 2015). Borehole IV is vertical and shallower than the others. It has 3 data loggers at depths of 0.10, 0.65 and 1.20 m (Numbered 10, 11 and 12, Tinti et al., 2015). The whole intervention area and the location of the 3 measurement points on Borehole III with respect to the underground cellar, are shown in *Figure 1*.

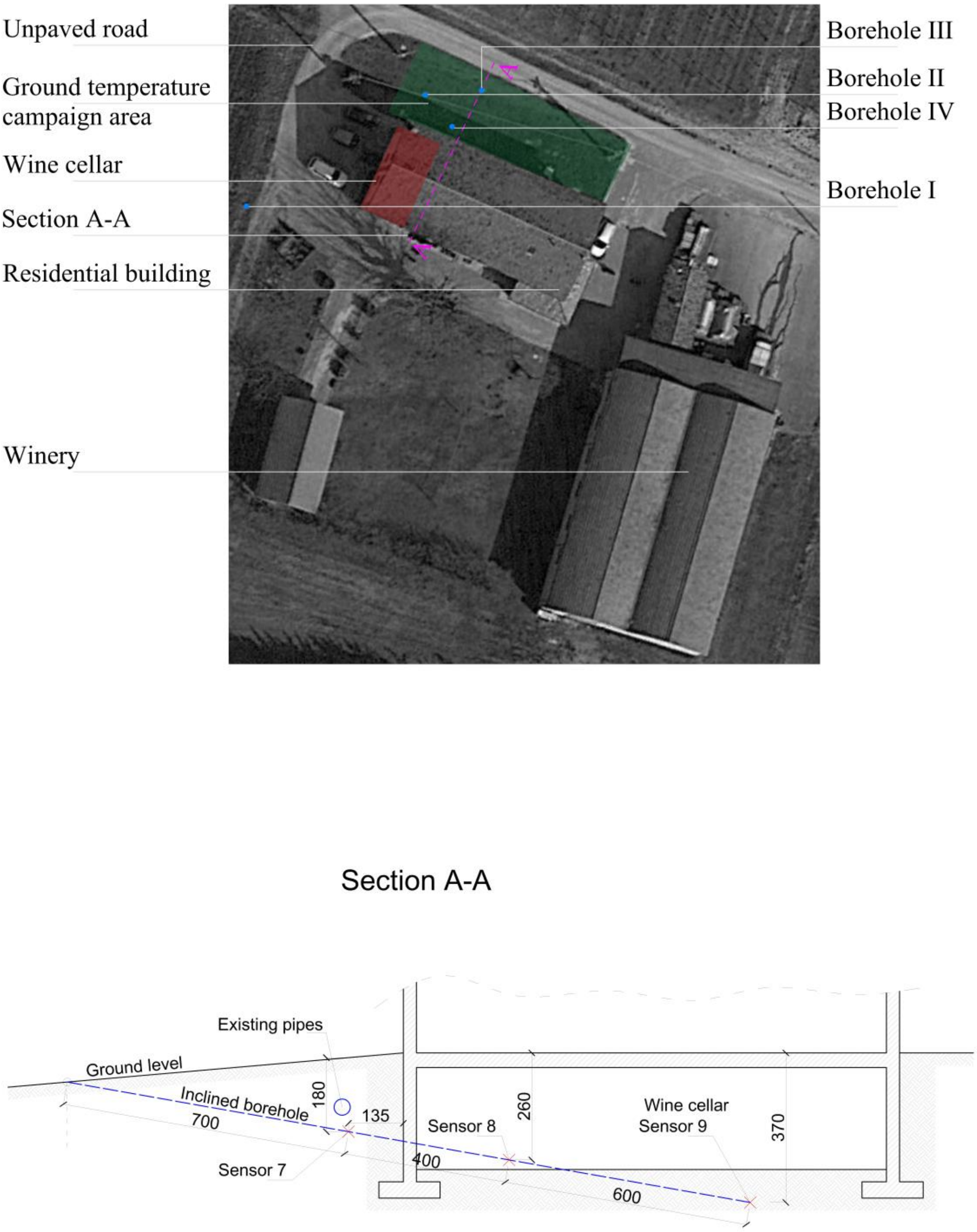

Figure 1. Intervention area (up) and vertical section of the underground cellar, with localization of the three measurement points (down).

The shallow underground of the whole area is prevalently composed of low moist clay down to a depth of 6 m, even lower in some places. Data sources are the geological investigations related to the installation of data loggers. All geological data were collected by the borehole data loggers.

The model domain implemented in *FEFLOW®* extends beyond the building itself for a total surface area of 60×60 m, a depth of 50 meters and 0.25 meters of boundary surface area, the latter chosen to guarantee a swathe of undisturbed ground around the boundary of the house. A tetrahedral mesh was used with refinement regions close to three observation points, corresponding to measurement points 7, 8 and 9. The finite elements generated range from $5 \cdot 10^{-2}$ m^2 in the zones close to the sensors to 5 m^2 from the building (*Figure 2*).

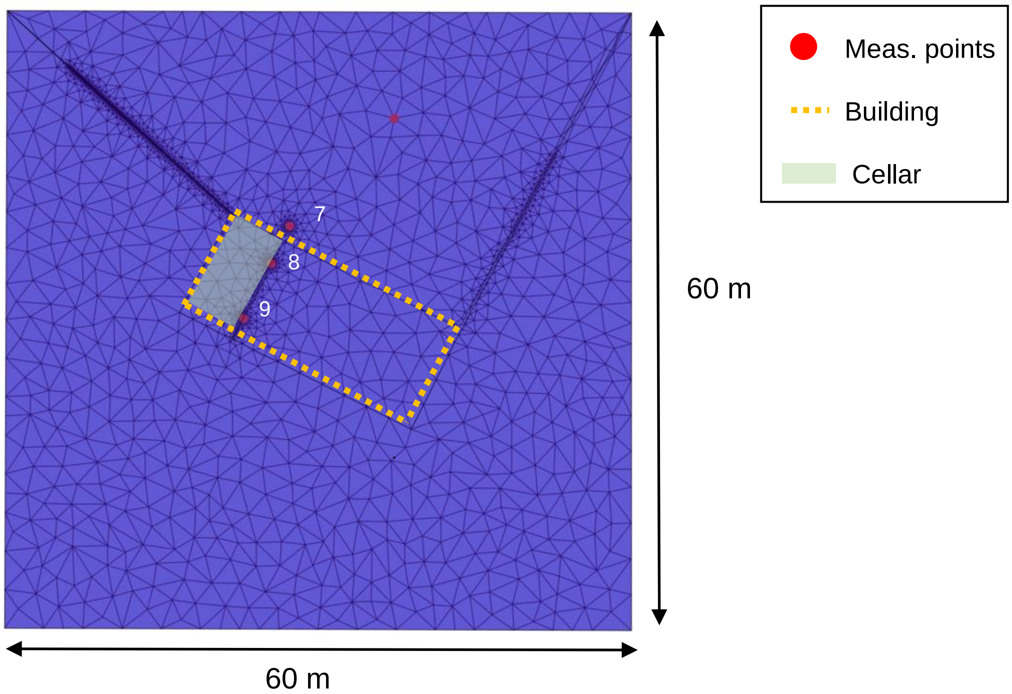

Figure 2. Mesh of the area chosen for the dynamic simulation.

A series of 18 layers was used to detail the geology of the area as well as a first buffer layer. Geological detail up to 50 m was obtained from the Geological Survey of the Emilia Romagna Region (*Figure 3*). The study does not consider groundwater flow in the two aquifers located respectively at 18 m and 30 m below the ground surface since their thermal impact is nil with respect to the intervention area (between 0.5 and 10 m below the ground surface).

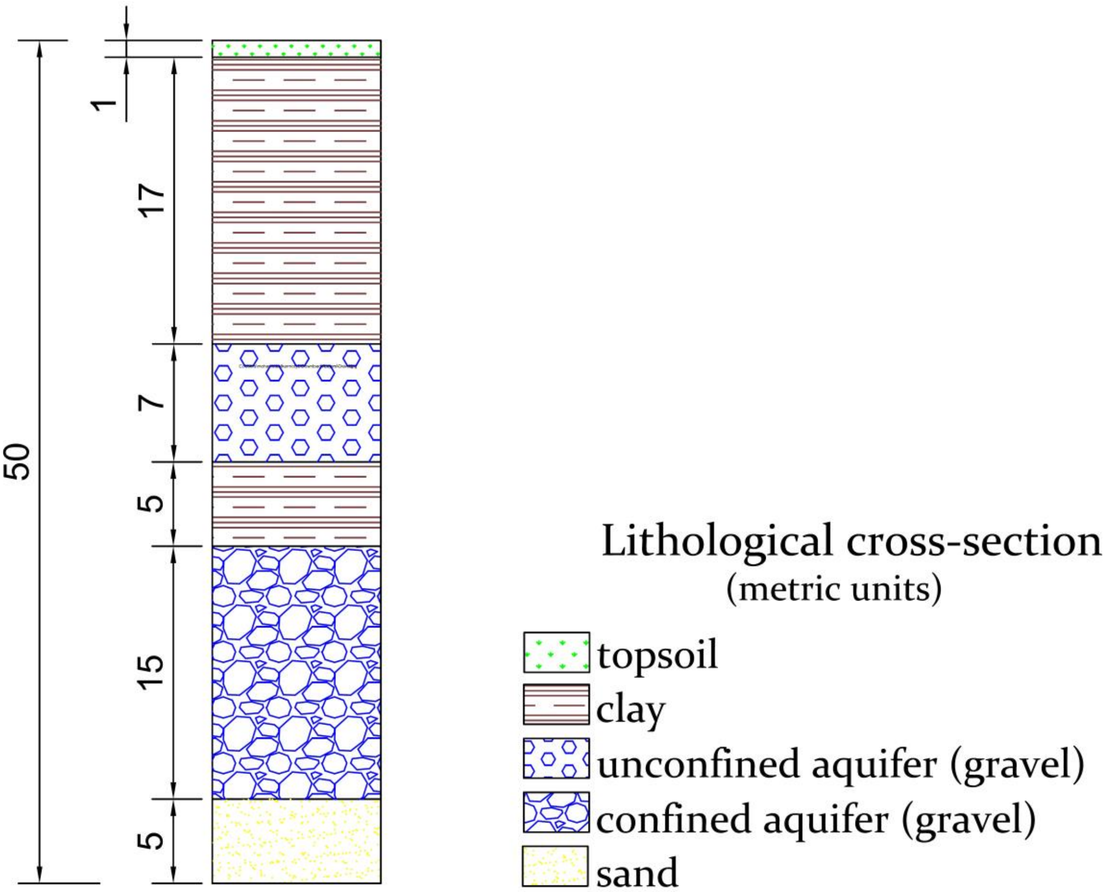

Figure 3: Lithological cross-section for the case study (from Tinti et al., 2017a).

Measurement points 7, 8 and 9, expressed in relation to the cellar and building walls, are given in *Table 2.* All of them are located in low moist clay.

Table 2. Localization of measurement points 7, 8 and 9.

Sensor number	**Depth (m)**	**Qualitative localization**	**Orthogonal distance from the building northern wall (m)**	**Geological layer number (refer to Table 4)**
7	1.8	Beside the building and cellar walls	+1.35	6
8	2.6	Under the building, beside the cellar wall	-2.57	7
9	3.7	Under the building, under the cellar	-8.47	9

2.3. Model boundaries: ground and building temperature

The basic equation for assessing vertical temperature (T_g) distribution at low depth is a function of the ambient temperature wave and the thermal properties of the ground (Kusuda and Achenbach, 1965). Since all the function variables are regionalized, the target variable is four dimensional, varying in space (*x,y,z*) and time (*t*). Since T_g has a sinusoidal behaviour, the year is usually given as a wave period.

Equation 1 summarizes the well-known distribution of temperatures in the subsoil at low depths (Baggs, 1985).

$$T_g(x,y,z,t) = T_{me}(x,y) - A_e(x,y)\cdot \exp\left[-z\cdot\sqrt{\left(\frac{\pi}{365\cdot\alpha(x,y,z)}\right)}\right]\cdot\cos\left[\frac{2\cdot\pi}{365}\cdot\left(t - t_{T_0}(x,y) - \frac{z}{2}\cdot\sqrt{\frac{365}{\pi\cdot\alpha(x,y,z)}}\right)\right] \quad 1.$$

Where:

T_g is the space-time varying underground temperature (°C),

T_{me} is the annual surface average temperature (°C),

A_e is the annual surface wave amplitude (°C),

t_{T0} is the time at minimum temperature (days),

α is the equivalent thermal diffusivity (m^2/days).

Although other parameters such as the vegetation coefficient, the insulation coefficients, and the geothermal heat flow, can be included in the analytical equation, we decided to omit these in the present work since our aim was to define settings to recreate the bulb-shaped volume of subsurface temperatures below a building in the numerical simulator without the inclusion of corrective coefficients. In addition, since the area of investigated was limited to the shallow layers, disregarding the contribution of geothermal heat flow was in this case an acceptable simplification.

Experimental temperature measurement in Boreholes I and II (Tinti et al., 2014) allowed estimation of ground thermal wave parameters by non-linear regression based on *Equation 1*. Parameters obtained by non-linear regression are summarized in *Table 3.*

Table 3. Entering parameters to estimate ground temperature in the survey area with the analytical method.

Yearly ambient temperature (°C)	**Yearly amplitude (°C)**	**Day of minimum temperature (days)**	**Ground thermal diffusivity (m^2/days)**
15.0	15.5	10th	0.0288

January 10th is statistically the day of minimum temperature in the climatic area of Bologna, so in the climatic wave it represents the position of the inflection point.

Since the ground was considered homogeneous in the survey area, no spatial variations were attributed to parameters. The temperature of the ground below the study area (i.e. from 18 m) was calculated also considering geological and hydrogeological variations, as reported in Tinti et al., 2017a. Since the effect of deep temperature on the surface layers is very limited, no further investigations were conducted during this study below 18 m. The temperatures indicated by Tinti et al., 2017a were used in the dynamic simulator as boundary and initial conditions. The baseline condition for each layer was that layer's average temperature on 1st January (starting date of the simulation) as shown in *Table 4*, while the Dirichletian boundary conditions at the borders of each layer were represented as the time-varying temperature evolution over the year. As no groundwater flow was considered, a Dirichletian boundary condition of 0 m hydraulic head was set for all the sides and layers of the model.

Table 4. Initial temperature conditions for each layer of the model.

Layer n°	Thickness (m)	Depth (m)	Initial temperature (°C)
2	0.25	0.25	4.67
3	0.25	0.50	6.24
4	0.50	1.00	7.80
5	0.50	1.50	10.44
6	0.50	2.00	12.51
7	0.50	2.50	13.47
8	0.50	3.00	14.96
9	1.00	4.00	15.85
10	2.00	6.00	16.45
11	2.00	8.00	16.10
12	2.00	10.00	15.58
13	2.00	12.00	15.52
14	6.00	18.00	15.66
15	7.00	25.00	15.93
16	5.00	30.00	15.37
17	15.00	45.00	15.84
18	5.00	50.00	15.60

The ground profile was defined based on the lithological section (*Figure 3*). Layers 2 to 4 are all part of the first lithological type (topsoil); layers 5 to 14 are part of the second lithological type (clay). Both were refined to obtain better representation of the superficial layers, which are mostly influenced by the external temperature. In contrast, layers 15 to 18 were defined according to the original thickness of each lithological type.

The basement of the two-storey building was considered as corresponding to the top of Layer 2. Since Layer 1 was considered an ambient temperature buffer, Layer 2 was considered as located at 0 m depth. The time-varying temperature over the year registered inside the building ($T_{building}$) at this 0 m depth was considered as the Dirichletian boundary. The basement of the wine ageing room was, on the other hand, placed at the top of Layer 8 (located at a depth of 3 m). The Dirichletian boundary condition at this depth was the time-varying temperature over the year registered in the wine room (T_{cellar}). *Figure 4* shows the reference temperatures inside the building and cellar over one year during the study.

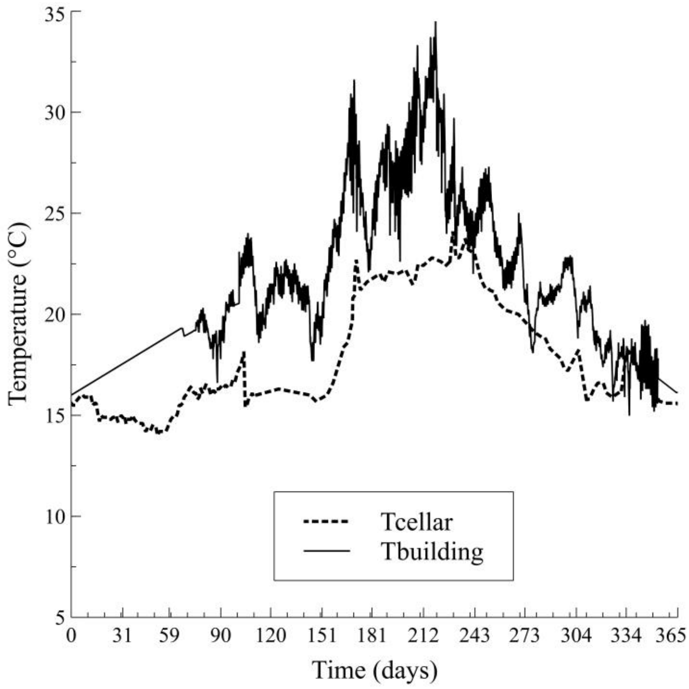

Figure 4. Internal temperature of building and cellar

The two temperature evolutions were used as wall temperature conditions in the simulation to express the heat effect of the building.

2.4. Model parameters: thermal conductivity, heat capacity and effective porosity

Each of the 18 layers was characterized in terms of thermal properties, namely thermal conductivity, thermal capacity, and effective porosity. Respective values are shown in *Table 5*.

For the specific case study, the value of thermal diffusivity was calculated through the multiyear measurement campaign up to a depth of 6 m. The value was later additionally verified by a Thermal Response Test (TRT) performed on a geothermal basket installed on site (Ferrari et al., 2016; Tinti et al., 2017b).

Other parameters were obtained on the basis of the relationship between thermal diffusivity and conductivity, as shown in Equation 2.

$$\alpha = \frac{\lambda}{\rho \cdot C}$$

2.

Where

λ is the equivalent thermal conductivity (W/(m·K)),

ρ is the density (kg/m^3),

C is the heat capacity (J/(kg·K)),

$\rho \cdot C$ is the volumetric heat capacity (J/(m^3·K)).

Lithology-based bibliographic values were taken for the layers deeper than 18 m below the ground surface (Tinti et al., 2017a). Effective porosity was set at 10% (i.e. low effective porosity, typical of low moist clay) down to the first aquifer (18 m deep), where it was increased up to 30%. Effective porosity was used in the simulation to estimate the amount of water in the aquifer and the quantity of air in the dry layers. This, together with the thermal conductivity and volumetric heat capacity provided for each of the lithologies generated the actual thermal properties of each layer.

Table 5. Thermal characteristics associated with the layers.

Layer n°	Thickness (m)	Depth (m)	Thermal conductivity (W/(m·K))	Volumetric heat capacity (MJ/(m^3·K))	Effective porosity (-)
2	0.25	0.25	0.50	1.0	0.1
3	0.25	0.50	0.65	1.5	0.1
4	0.50	1.00	0.65	1.5	0.1
5	0.50	1.50	0.65	1.5	0.1
6	0.50	2.00	0.65	1.5	0.1
7	0.50	2.50	0.65	1.5	0.1
8	0.50	3.00	0.65	1.5	0.1
9	1.00	4.00	0.65	1.5	0.1
10	2.00	6.00	0.65	1.5	0.1
11	2.00	8.00	0.65	1.5	0.1
12	2.00	10.00	0.65	1.5	0.1
13	2.00	12.00	0.65	1.5	0.1
14	6.00	18.00	0.65	1.5	0.1
15	7.00	25.00	1.80	2.4	0.3
16	5.00	30.00	1.00	1.6	0.3
17	15.00	45.00	1.80	2.4	0.3
18	5.00	50.00	2.40	2.4	0.3

A thermal conductivity of 0.35 W / (m·K) was assigned to the building walls and floors. This represents the characteristic thermal conductivity of a hollow concrete slab with a high degree of insulation.

3. Results

The above model, implemented in *FEFLOW®*, was run for 1825 days under the boundary and initial conditions described. The initial time step was set at 0.5 days and subsequently defined automatically by the convergence of the equations. Local temperatures at the measurements points were retrieved from the simulation each day and compared with the on-site measurements and estimated data based on non-linear regression on *Equation 1*. The undisturbed ground temperature of each layer was recorded along a vertical profile at observation points positioned one on top of the other at 15 m from the building (where the heat island effect is negligible). Since the new dynamic boundary conditions settle after 2 years of simulation, comparison between simulated and estimated natural ground temperatures can be made taking either the 3^{rd}, 4^{th} or 5^{th} year of simulation (*Equation 1*). In this study we carried out the comparison on the basis of simulated temperatures of the 5^{th} year.

The match between simulated and estimated values of space-time varying ground temperature was obtained in all parts of the domain (including below the building and beside the cellar) using the following settings:

- Tetrahedral mesh refined around sensor positions, where observation points were defined;
- Initial temperatures of the different layers set equal to the average 1^{st} January temperature;
- Dirichletian boundary conditions for the temperature of each layer equal to the time-varying evolution of each layer temperature over the year;
- Dirichletian boundary condition for building wall temperature equal to the time-varying temperature registered over the year inside the building;
- Dirichletian boundary condition for cellar wall temperature equal to the time-varying temperature registered over the year inside the cellar;
- Dirichletian boundary condition of 0 m hydraulic head set throughout the model.

3.1. Reconstruction of undisturbed underground temperature

The comparison between simulated and estimated values of ground temperature evolution is presented in *Figure 5.* Ground temperatures at the different depths were estimated using non-linear regression based on *Equation 1,* and validated at the different depths (2, 4 and 6 m) against those measured (Tinti et al., 2014).

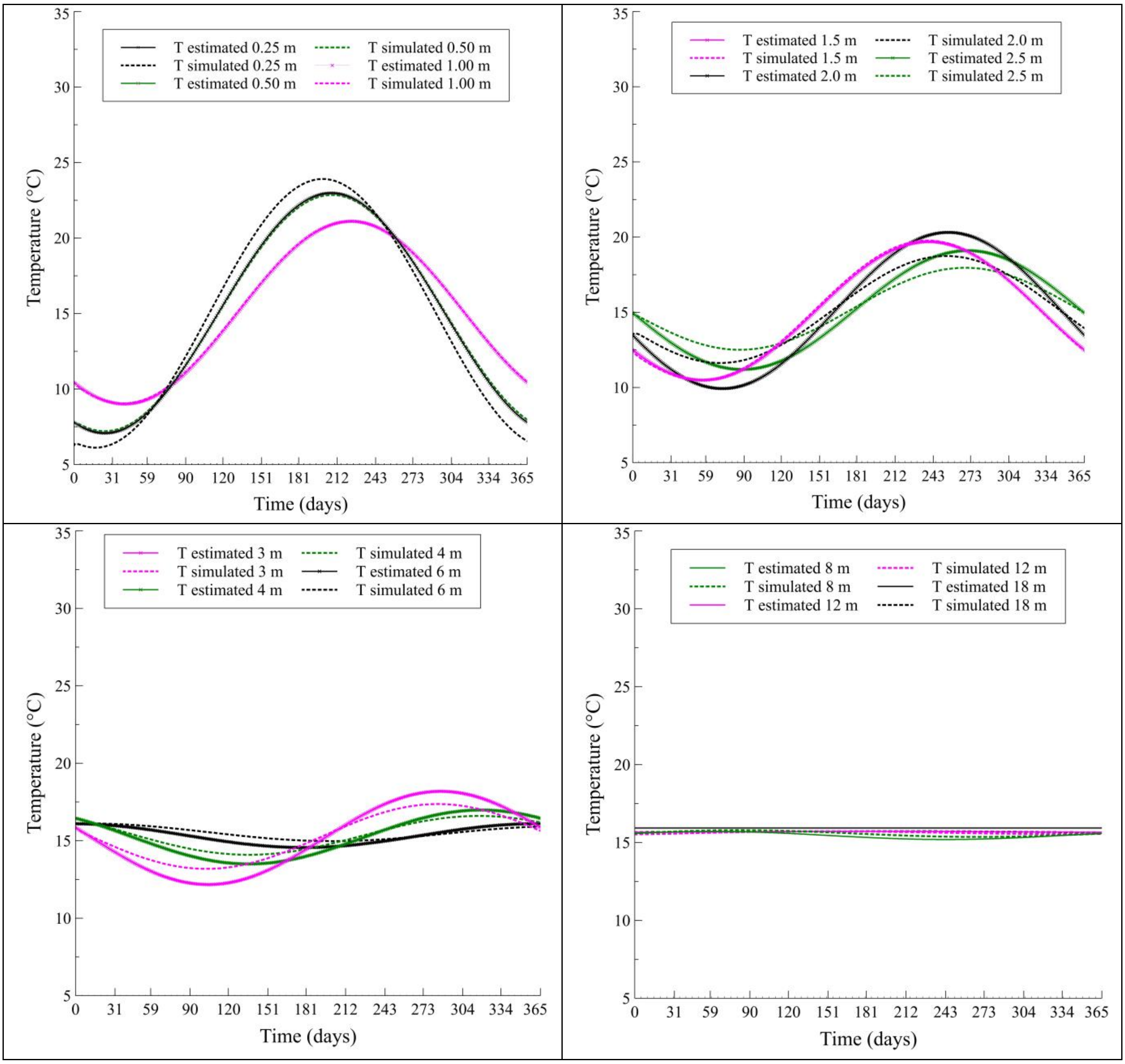

Figure 5. Comparison between simulated and estimated temperatures at different depths.

Table ***6*** reports the average simulated wave error with respect to that estimated at each depth. The values estimated with non-linear regression are considered as reference values. Error tends to decrease with depth because the temperature becomes more homogeneous.

Table 6. Maximum, minimum and average error of the simulated ground temperature at different depths compared to the estimated values by non-linear regression of Equation 1 on measurement points (Tinti et al., 2014).

Depth (m)	**Maximum Relative Error (%)**	**Minimum Relative Error (%)**	**Average Relative Error (%)**
0.00	6.1%	0.0%	2.2%
0.25	5.5%	0.0%	2.1%
0.50	5.1%	0.0%	2.3%
1.00	4.7%	0.0%	2.3%
1.50	17.8%	0.1%	9.3%
2.00	13.4%	0.0%	7.3%
2.50	10.3%	0.0%	5.8%
3.00	6.3%	0.0%	3.6%
4.00	4.4%	0.0%	2.5%
6.00	1.9%	0.0%	0.9%
8.00	0.7%	0.0%	0.3%
10.00	0.4%	0.0%	0.2%
12.00	1.5%	1.4%	1.5%
18.00	2.1%	1.9%	2.0%

3.2. Reconstruction of sensor recorded temperatures.

The temperatures measured at points 7, 8 and 9 were compared with the products of the simulation. Since the three investigation points come within the impact area affected by building heat loss, the values returned at these points do not follow the natural ground thermal state. *Figure 6* shows the comparison.

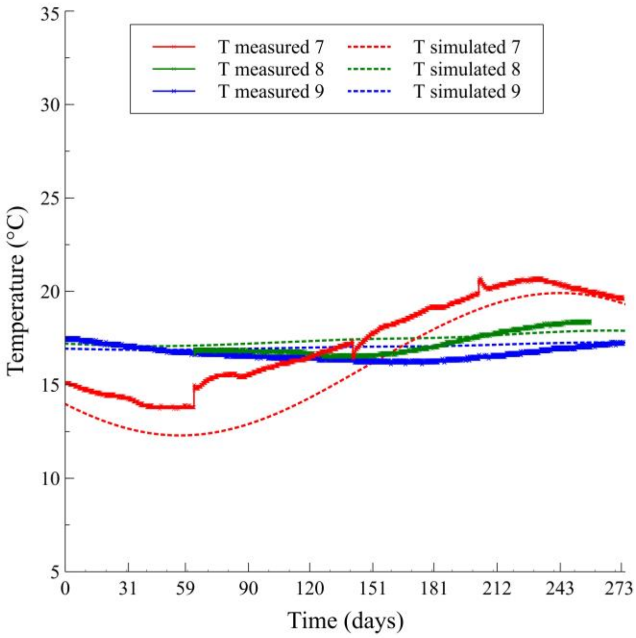

Figure 6. Comparison between simulated and measured temperature values beside and below the building at measurement points 7 (1.8 m), 8 (2.6 m) and 9 (3.7 m).

The comparison led to the average error presented in *Table 7.*

Table 7. Maximum, minimum and average error of the simulated sensor-based temperature compared to the actual values measured.

Sensor	**Depth**	**Maximum Relative Error**	**Minimum Relative Error**	**Average Relative Error**
7	1.8 m	19.4%	0.8%	9.0%
8	2.6 m	6.1%	0.1%	2.4%
9	3.7 m	5.3%	0.1%	2.8%

The low average error shows that the settings were correctly chosen to include the building's thermal contribution in the dynamic simulator.

3.3. Simulation of building thermal effect on the ground

Having calibrated the model by comparing simulated and measured data, it was then possible to simulate the entire ground thermal behaviour as affected by the building over time. The results for four characteristic periods of January, April, July and October are given in section *B-B* of *Figure 7*. Ground temperature evolution is shown in *Figure 8.*

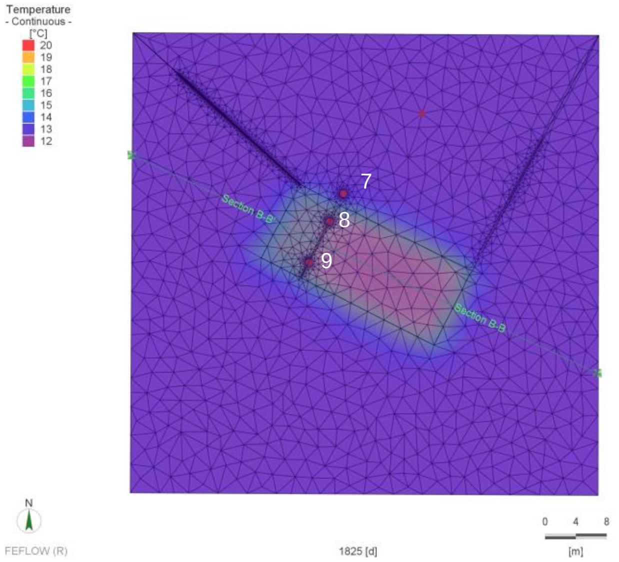

Figure 7 Simulated area and definition of Section B-B.

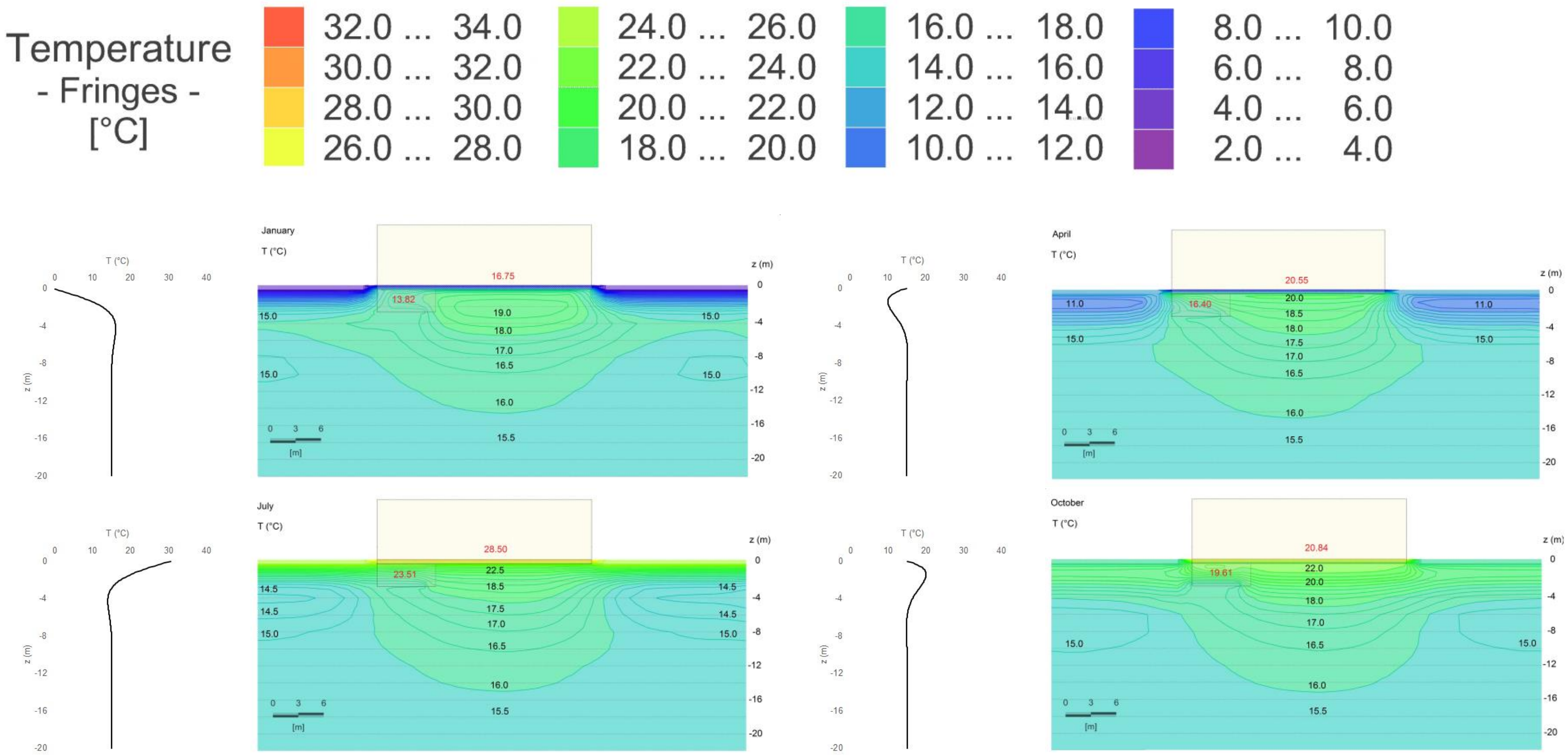

Figure 8. Section B-B showing ground thermal behaviour affected by the presence of the building and cellar in the characteristic months of January, April, August and October. For each month, the following items are shown: temperature isolines in the ground (black numbers), average temperature in the above ground building and the cellar (red numbers), temperature profile used as boundary condition (black line).

Simulation of ground temperature evolution under the building follows the bulb-shaped pattern described consistently in the literature and presented in the introduction to this paper. Temperature variation with depth is notably vertically dampened compared with the undisturbed ground, with no relevant changes occurring over time. This is because the building acts as an insulator against the external weather. Below the building, at depths from 2 to 8 m, temperature remains constant throughout the year at around 17-18°C. In contrast, temperatures around the building down to 4 m depth, in winter, vary from 2 to 15 °C, while, in summer, vary from 28 to 14.5°C. From 4 down to 8 m, there is a transitional zone, with very low temperature variations along the year, while below 8 m temperature remains constant in time.

The numerical simulation also evidences the thermal contribution of the indoor air temperature of the cellar, which slightly affects the temperatures of its surroundings.

Being validated by the measurements taken, the simulation values may be used in the design of energy geostructures and ground heat exchangers when these are located below buildings.

Results can be used both directly in *FEFLOW*® as initial conditions for further simulations of geothermal energy exploitation or extrapolated for the dedicated design of energy geostructures and ground heat exchanger fields.

Since the heat exchange rates of ground heat exchangers in winter and summer are proportional to initial ground temperature, it follows that exchanger systems for standard heating and cooling loads will be more profitable below a building than underneath an uncovered area. So correct simulation in all grid nodes improves the quality of design. Considering the correct thermal impact of buildings on the ground should lead to more precise forecasts of geothermal energy exploitation rates for heating and cooling needs.

4. Conclusions

The study defined optimal settings to reconstruct the time-space varying temperature field deriving from the presence of a building in a dynamic simulator. The settings were calibrated performing numerical simulation and comparing the results with ground temperature values measured on site in a rural area beside and below a detached building. As far as the authors are aware, this is one of the few studies of its kind. It could pave the way for better thermal behaviour simulation, which would lead to improved energy geostructures and ground heat exchanger design. In particular, the results of this paper are especially pertinent for ground heat exchanger design in urban areas, where the presence of buildings can considerably affect thermal system performance. This is especially the case of energy piles with absorption pipes installed below buildings, where standard climate-dependent ground thermal conditions do not apply. Moreover, energy pile length is usually limited to a few meters below any building, with the result that thermal losses from buildings will have a large impact on energy performance. The study further underlines that the exploitable energy used by shallow ground heat exchangers located in urban areas is only in part 'natural' (renewable geothermal and solar energy) since heat recovery of energy losses from buildings and districts (subsurface urban heat island effect) make up a sizeable component of the energy available to these systems. Further studies will be performed to quantify this contribution in the short and long term, both for energy geostructures located below single buildings and for ground heat exchanger fields located in an urban area, with estimation and simulation of the effect of multiple buildings on ground heat exchanger fields.

Acknowledgements

The Authors wish to thank the Branchini 1858 winery of Toscanella di Dozza (BO), Italy for their collaboration during of the monitoring and experimental trials. Thanks also go to all the co-workers and technicians of University of Bologna who over the years have helped install, improve and maintain the monitoring system.

References

Al-Khoury R, Bonnier PG and Brinkgreve R.B.J. (2005) Efficient finite element formulation for geothermal heating systems. Part I: steady state. International Journal for Numerical Methods in Engineering **63(7)**: 988 - 1013

Al-Khoury R and Bonnier PG (2006) Efficient finite element formulation for geothermal heating systems. Part II: transient. International Journal for Numerical Methods in Engineering. **67(5)**:725 - 745.

Al-Zyoud S., Rühaak W. and Sass I. (2014) Dynamic numerical modelling of the usage of groundwater for cooling in north east Jordan. A geothermal case study. Renewable Energy **62**: 63 - 72

Allen A., Milenic D. and Sikora P. (2003) Shallow gravel aquifers and the urban ‘heat island’ effect: a source of low enthalpy geothermal energy. Geothermics **32(4)**: 569 – 578.

Arola T. and Korkka-Niemi K. (2014) The effect of urban heat islands on geothermal potential: examples from Quaternary aquifers in Finland. Hydrogeology Journal **22(8)**: 1953 – 1967, https://doi.org/10.1007/s10040-014-1174-5.

Baggs S.A. (1985) Remote prediction of ground temperature in Australian soils and mapping its distribution. Solar Energy **30(4)**: 351 –366.

Bandos T.V., Montero A., Fernandez E., Santander J.L.G., Isidro J.M. et al. (2009) Finite line-source model for borehole heat exchangers: effect of vertical temperature variations. Geothermics **38(2)**: 263 - 270.

Barbaresi A., Torreggiani D., Benni S. and Tassinari P. (2014) Underground cellar thermal simulation: definition of a method for modelling performance assessment based on experimental calibration. Energy and Buildings **76**: 363–372.

Barbaresi A., Torreggiani D., Benni S. and Tassinari P. (2015) Indoor air temperature monitoring: A method lending support to management and design tested on a wine-aging room. Building and Environment **86**: 203 – 210.

Barla M., Di Donna A. and Baralis M. (2018) City-scale analysis of subsoil thermal conditions due to geothermal exploitation. Environmental Geotechnics, ahead of print. https://doi.org/10.1680/jenge.17.00087.

Benni S., Tinti F., Barbaresi A., Ferrari M., Bruno R. et al. (2016) Experimental models of underground temperature for decision making in wine cellar design. In *Proceedings of 44th International Symposium on Agricultural Engineering.* (Kovačev I. and Zrnčić H. (eds)). Sveučilište u Zagrebu, Agronomski fakultet, Zavod za mehanizaciju poljoprivrede, Zagreb, HR, pp. 487 - 498.

Bornstein R.D. (1968) Observation of the Urban Heat Island effect in New York City. Journal of Applied Meteorology **7(4**): 575 - 581.

Cermak, V., and Rybach, L. (1979) *Terrestrial heat flow in Europe*. Springer Verlag, ISBN 10:3540094407/ISBN 13:978354009440.

Claesson J. and Hagentoft C-E. (1991) Heat loss to the ground from a building – I. General theory. Building and Environment **26(2)**: 95-208.

Ferguson G. and Woodbury A.D. (2004) Subsurface heat flow in an urban environment. Journal of Geophysical Research **109(B2)**: B02402.

Ferguson G. and Woodbury A. D. (2007) Urban heat island in the subsurface. Geophysical Research Letters, **34(23)**: L23713.

Ferrari M., Barbaresi A., Tinti F., Brunelli D., Benni S., Verdecchia A. Bedeschi E., Bruno R., Tassinari P. (2016) Performance evaluation of a homemade cylindrical basket heat exchanger, by a multi-sensors monitoring campaign. In *Proceedings of European Geothermal Energy Conference 2016*. EGEC, Brussels, B. pp. 1-10.

Focaccia S. (2013) Thermal response test numerical modeling using a dynamic simulator. Geothermal Energy **1(3)**: pp. 12

Focaccia S., Tinti F., Monti F., Amidei S. and Bruno R. (2016) Shallow geothermal energy for industrial applications: A case study. Sustainable Energy Technologies and Assessments **16**: 93 - 105,

Hagentoft C-E and Claesson J. (1991) Heat loss to the ground from a building – II. Slab on the ground. Building and Environment **26(4)**: 395 - 403.

Headon J., Banks D., Waters A. and Robinson V. K. (2009) Regional distribution of ground temperature in the Chalk aquifer of London, UK. Quarterly Journal of Engineering Geology & Hydrogeology **42(3)**: 313 - 323.

Herbert A. S. and Chillingworth G. (2013) Thermal modelling of large scale exploitation of ground source energy in urban aquifers as a resource management tool. Applied Energy **109**: 94–103.

Huang S., Taniguchi M., Yamano M. and Wang C. H. (2009) Detecting urbanization effects on surface and subsurface thermal environment-a case study of Osaka. Science of the Total Environment **407(9)**: 3142 - 3152

Kurevija T. and Vulin D. (2010) Determining undisturbed ground temperature as part of shallow geothermal resources assessment. Rudarsko-Geolosko-Naftni Zbornik **22**: 27-36.

Kusuda T. and Achenbach P. (1965) Earth temperature and thermal diffusivity at selected stations in the United States, ASHRAE Transactions **71**: 61 - 75.

Landsberg, H. E. (1981) The Urban Climate. International Geophysics Series **28**: 275.

Mazarron F.R., Cid-Falceto J. and Canas I. (2012) Ground thermal inertia for energy efficient building design: a case study on food industry. Energies **5(2)**: 227 - 242.

Menberg K., Bayer P., Zosseder K., Rumohr S. and Blum P. (2013): Subsurface urban heat islands in German cities. Science of Total Environment **442**: 123–133.

Oke, T. R. (1982) The energetic basis of the urban heat island Quarterly Journal of the Royal Meteorological Society **108(455)**: 1 – 24

Pouloupatis P.D., Florides G., Tassou S. (2011) Measurements of ground temperatures in Cyprus for ground thermal applications. Renewable Energy **36(2)**: 804–814.

Poulsen S.E., Balling N. and Nielsen S.B. (2015) A parametric study of the thermal recharge of low enthalpy geothermal reservoirs. Geothermics **53**: 464-478.

Pruess K. and Garcia J., (2002) Multiphase flow dynamics during CO_2 disposal into saline aquifers. Environmental Geology **42(2-3)**: 282 - 295.

Rees S.W., Adjali M.H., Zhou Z., Davies M. and Thomas H.R. (2000) Ground heat transfer effects on the thermal performances of earth-contact structures. Renewable and Sustainable Energy Reviews **4(3)**: 213 - 265.

Rivera J.A., Blumm P. and Bayer P. (2017) Increased ground temperatures in urban areas: Estimation of the technical geothermal potential. Renewable Energy **103**: 388 – 400.

Taniguchi M, Uemura T. and Jago-on K. (2007) Combined effects of urbanization and global warming on subsurface temperature in four Asian cities. Vadose Zone Journal **6**: 591–596.

Tinti F., Barbaresi A., Benni S., Torreggiani D., Bruno R. et al. (2014) Experimental analysis of shallow underground temperature for the assessment of energy efficiency potential of underground wine cellars. Energy and Buildings **80**: 451 - 460.

Tinti F., Barbaresi A., Benni S., Torreggiani D. Bruno R. et al. (2015) Experimental analysis of thermal interaction between wine cellar and underground. Energy and Buildings **104**: 275 - 286.

Tinti, F., Barbaresi, A., Ferrari, M., Elkarmoty, M., Torreggiani, D., et al. (2017a) Experimental calibration of underground heat transfer models under a winery building in a rural area. Rudarsko Geolosko Naftni Zbornik **32(3)**: 15 - 22.

Tinti, F. Barbaresi, A., Torreggiani, D., Brunelli, D., Ferrari, M. et al. (2017b) Evaluation of efficiency of hybrid geothermal basket/air heat pump on a case study winery based on experimental data. Energy and Buildings **151**: 365 - 380.

Wu Y., Gan G., Verhoef A., Vidale P. L., Garcia Gonzalez R. (2010) Experimental measurement and numerical simulation of horizontal-coupled Slinky Ground Source Heat Exchangers. Applied Thermal Engineering **30(16)**: 2574 – 2583.

Yalcin T. and Yetemen O. (2009) Local warming of groundwaters caused by the urban heat island effect in Istanbul, Turkey. Hydrogeology Journal **17(5)**: 1247 - 1255.

Zhao C., Wang Y., Chen X. and Li B. (2005) Simulation of the effects of groundwater level on vegetation change by combining FEFLOW software. Ecological Modelling **187(2-3)**: 341-351.

Zhu K., Blum P., Ferguson G., Balke K.-D. and Bayer P. (2010) The geothermal potential of urban heat islands. Environmental Research Letters **5(4)**: pp. 5.

Figure captions

Figure 1. Intervention area (up) and vertical section of the underground cellar, with localization of the three measurement points (down).

Figure 2. Mesh of the area chosen for the dynamic simulation.

Figure 3: Lithological cross-section for the case study (from Tinti et al., 2017a)

Figure 4. Internal temperature of building and cellar

Figure 5. Comparison between simulated and estimated temperatures at different depths

*Figure 6. Comparison between simulated and measured temperature values beside and below the building at measurement points 7 (1.8 m)**,** 8 (2.6 m) and 9 (3.7 m).*

Figure 7 Simulated area and definition of Section B-B.

Figure 8. Section B-B showing ground thermal behaviour affected by the presence of the building and cellar in the characteristic months of January, April, August and October. For each month, the following items are shown: temperature isolines in the ground (black numbers), average temperature in the above ground building and the cellar (red numbers), temperature profile used as boundary condition (black line).

Table captions

Table 1: Key building features.

Table 2. Localization of measurement points 7, 8 and 9.

Table 3. Entering parameters to estimate ground temperature in the survey area with the analytical method.

Table 4. Initial temperature conditions for each layer of the model.

Table 5. Thermal characteristics associated with the layers.

*Table 6. Maximum, minimum and average error of the simulated ground temperature at different depths compared to the estimated values by non-linear regression of Equation 1 on measurement points (Tinti et al., 2014)***.**

Table 7. Maximum, minimum and average error of the simulated sensor-based temperature compared to the actual values measured.

Tables

Table 1: *Key building features.*

	Two-storey building	Wine-ageing room
Width	9.8 m	5.6 m
Length	20.5 m (above ground) + 5.6 m (above cellar)	9.8 m
Height	7.3 m (borders), 8.4 m (centre)	2.6 m (underground)
Walls	25.0 cm thick masonry	25.0 cm thick masonry
Floor	30.0 cm hollow concrete slab	20.0 cm concrete slab
Ceiling	-	30.0 cm hollow concrete slab
Air conditioning	Heating and natural ventilation	Natural ventilation

Table 2. Localization of measurement points 7, 8 and 9.

Sensor number	Depth (m)	Qualitative localization	Orthogonal distance from the building northern wall (m)	Geological layer number (refer to Table 4)
7	1.8	Beside the building and cellar walls	+1.35	6
8	2.6	Under the building, beside the cellar wall	-2.57	7
9	3.7	Under the building, under the cellar	-8.47	9

Table 3. Entering parameters to estimate ground temperature in the survey area with the analytical method.

Yearly ambient temperature (°C)	Yearly amplitude (°C)	Day of minimum temperature (days)	Ground thermal diffusivity (m^2/days)
15.0	15.5	10th	0.0288

Table 4. Initial temperature conditions for each layer of the model.

Layer n°	Thickness (m)	Depth (m)	Initial temperature (°C)
2	0.25	0.25	4.67
3	0.25	0.50	6.24
4	0.50	1.00	7.80
5	0.50	1.50	10.44
6	0.50	2.00	12.51
7	0.50	2.50	13.47
8	0.50	3.00	14.96
9	1.00	4.00	15.85
10	2.00	6.00	16.45
11	2.00	8.00	16.10

12	2.00	10.00	15.58
13	2.00	12.00	15.52
14	6.00	18.00	15.66
15	7.00	25.00	15.93
16	5.00	30.00	15.37
17	15.00	45.00	15.84
18	5.00	50.00	15.60

Table 5. Thermal characteristics associated with the layers.

Layer n°	Thickness (m)	Depth (m)	Thermal conductivity (W/(m·K))	Volumetric heat capacity (MJ/(m^3·K))	Effective porosity (-)
2	0.25	0.25	0.50	1.0	0.1
3	0.25	0.50	0.65	1.5	0.1
4	0.50	1.00	0.65	1.5	0.1
5	0.50	1.50	0.65	1.5	0.1
6	0.50	2.00	0.65	1.5	0.1
7	0.50	2.50	0.65	1.5	0.1
8	0.50	3.00	0.65	1.5	0.1
9	1.00	4.00	0.65	1.5	0.1
10	2.00	6.00	0.65	1.5	0.1
11	2.00	8.00	0.65	1.5	0.1
12	2.00	10.00	0.65	1.5	0.1
13	2.00	12.00	0.65	1.5	0.1
14	6.00	18.00	0.65	1.5	0.1
15	7.00	25.00	1.80	2.4	0.3
16	5.00	30.00	1.00	1.6	0.3
17	15.00	45.00	1.80	2.4	0.3
18	5.00	50.00	2.40	2.4	0.3

Table 6. Maximum, minimum and average error of the simulated ground temperature at different depths compared to the estimated values by non-linear regression of Equation 1 on measurement points (Tinti et al., 2014).

Depth (m)	Maximum Relative Error (%)	Minimum Relative Error (%)	Average Relative Error (%)
0.00	6.1%	0.0%	2.2%
0.25	5.5%	0.0%	2.1%
0.50	5.1%	0.0%	2.3%
1.00	4.7%	0.0%	2.3%
1.50	17.8%	0.1%	9.3%
2.00	13.4%	0.0%	7.3%
2.50	10.3%	0.0%	5.8%
3.00	6.3%	0.0%	3.6%
4.00	4.4%	0.0%	2.5%
6.00	1.9%	0.0%	0.9%
8.00	0.7%	0.0%	0.3%
10.00	0.4%	0.0%	0.2%
12.00	1.5%	1.4%	1.5%
18.00	2.1%	1.9%	2.0%

Table 7. Maximum, minimum and average error of the simulated sensor-based temperature compared to the actual values measured.

Sensor	Depth	Maximum Relative Error	Minimum Relative Error	Average Relative Error
7	1.8 m	19.4%	0.8%	9.0%
8	2.6 m	6.1%	0.1%	2.4%
9	3.7 m	5.3%	0.1%	2.8%

1a

Click here to access/download;Figure;Figure1a.jpg

1b

Click here to access/download;Figure;Figure1b.jpg

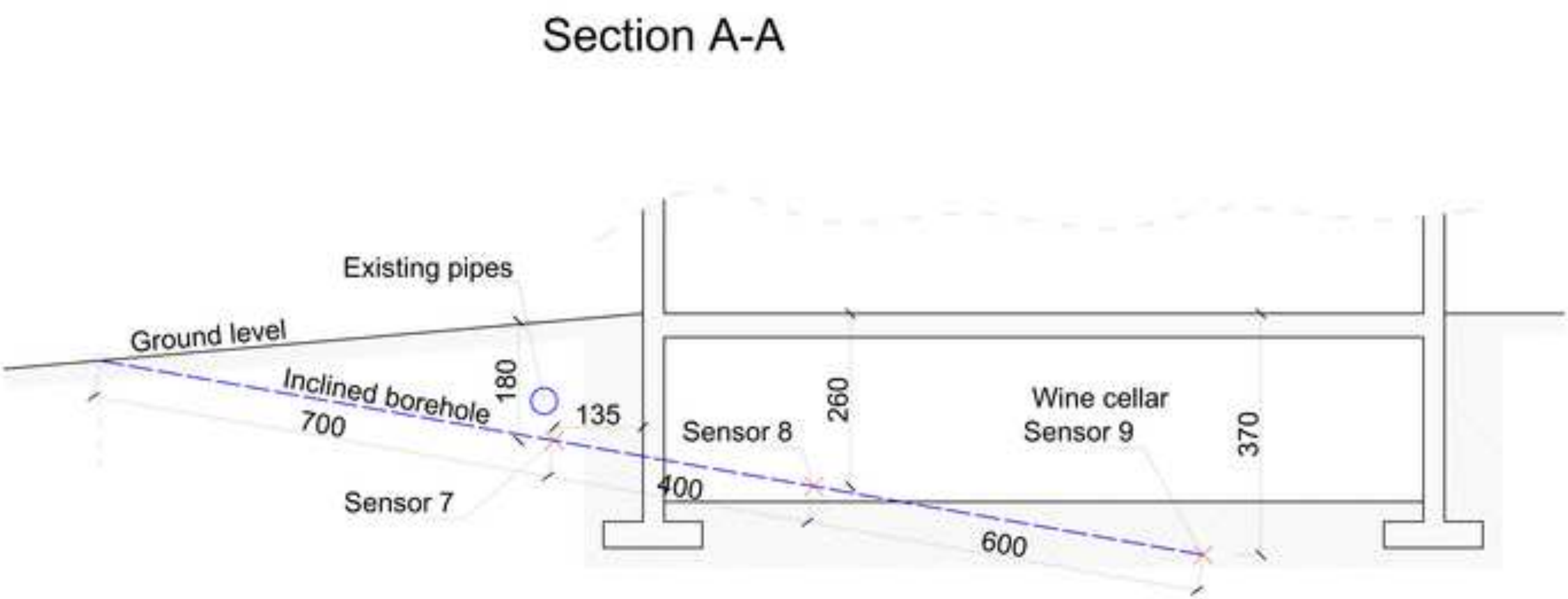

2

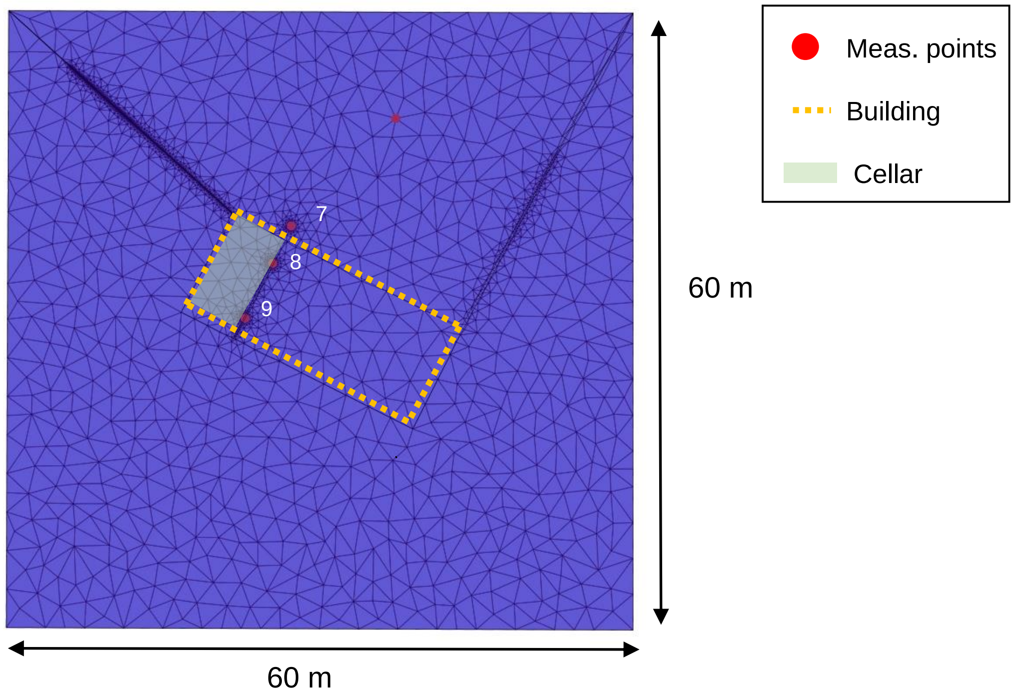

Click here to access/download;Figure;Figure3.jpg

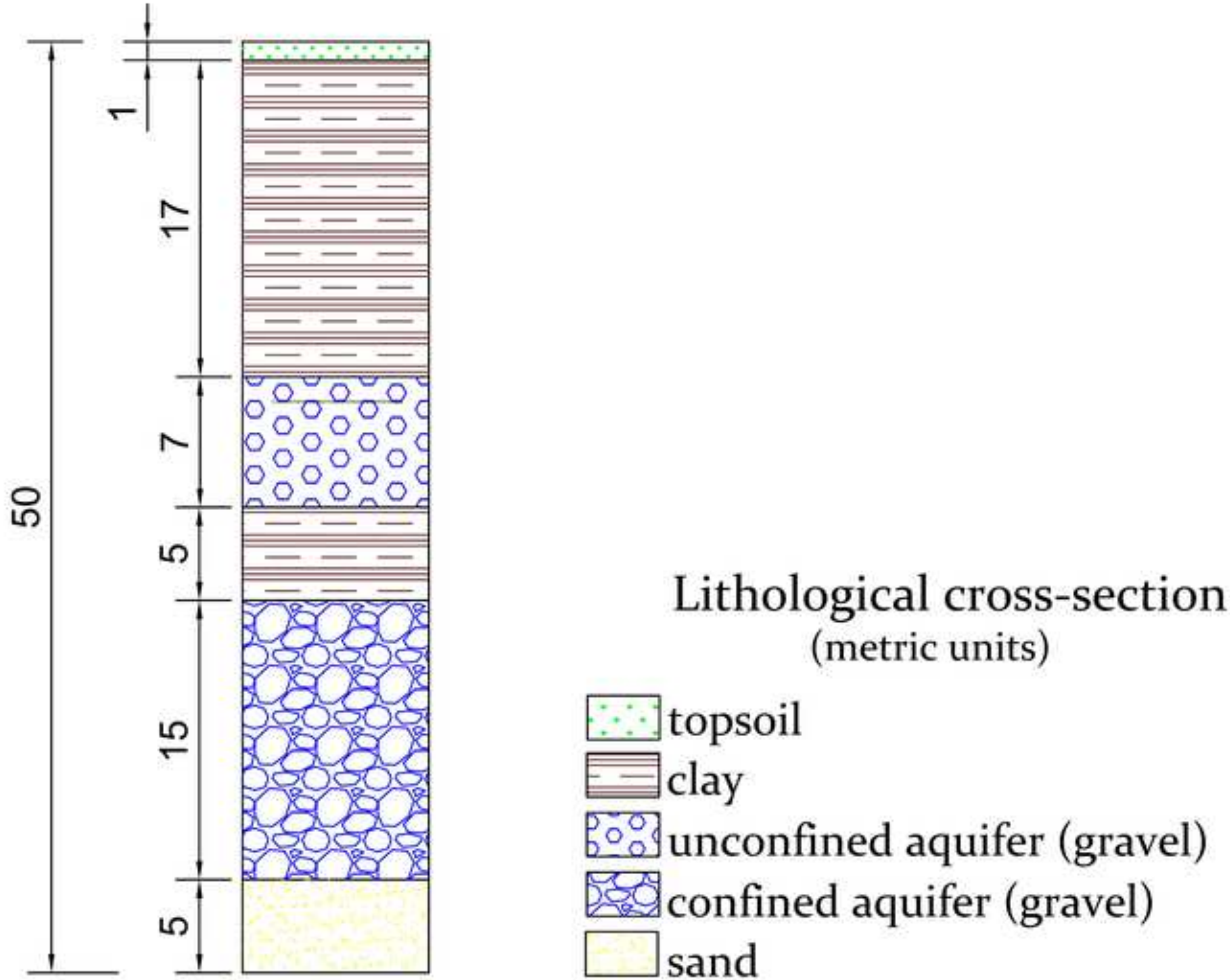

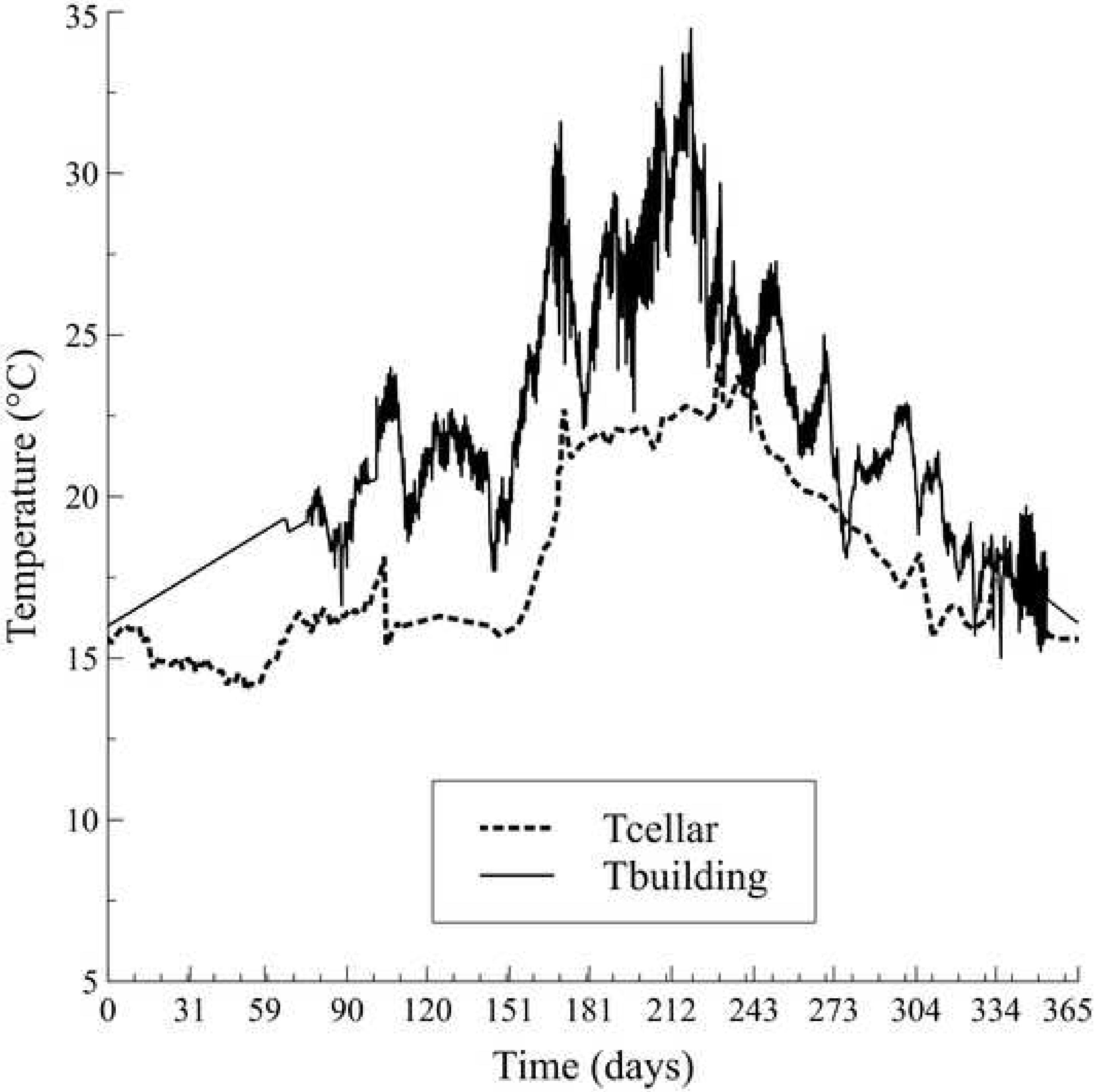
Temperature (°C)
35
30
25
20
15
10
5
0
31
59
90
120
151
181
212
243
273
304
334
365
Time (days)
Tcellar
Tbuilding

5a

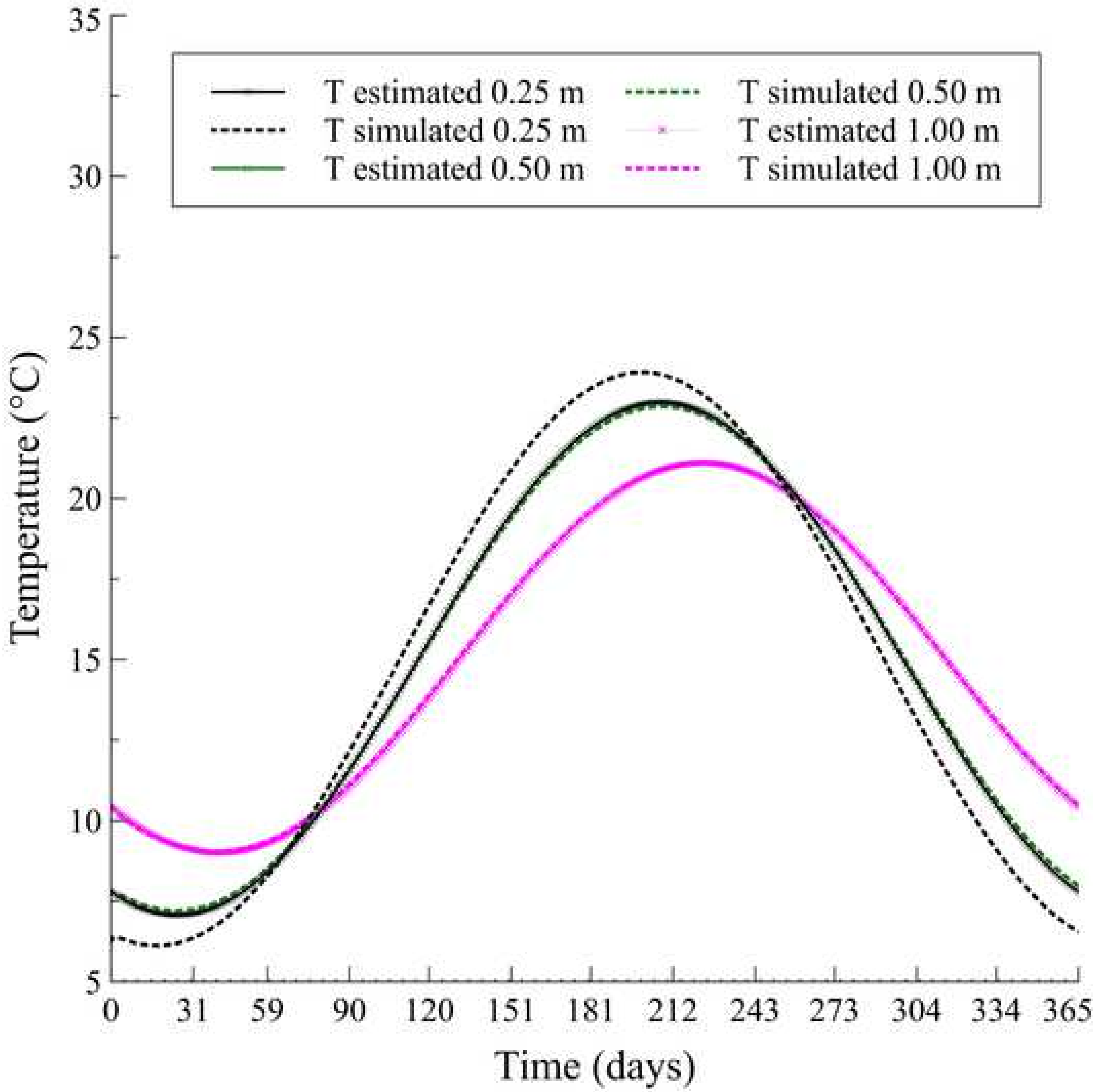
T estimated 0.25 m
T simulated 0.25 m
T estimated 0.50 m
T simulated 0.50 m
T estimated 1.00 m
T simulated 1.00 m
Temperature (°C)
Time (days)
35
30
25
20
15
10
5
0
31
59
90
120
151
181
212
243
273
304
334
365

5b

Click here to access/download;Figure;Figure5b.jpg

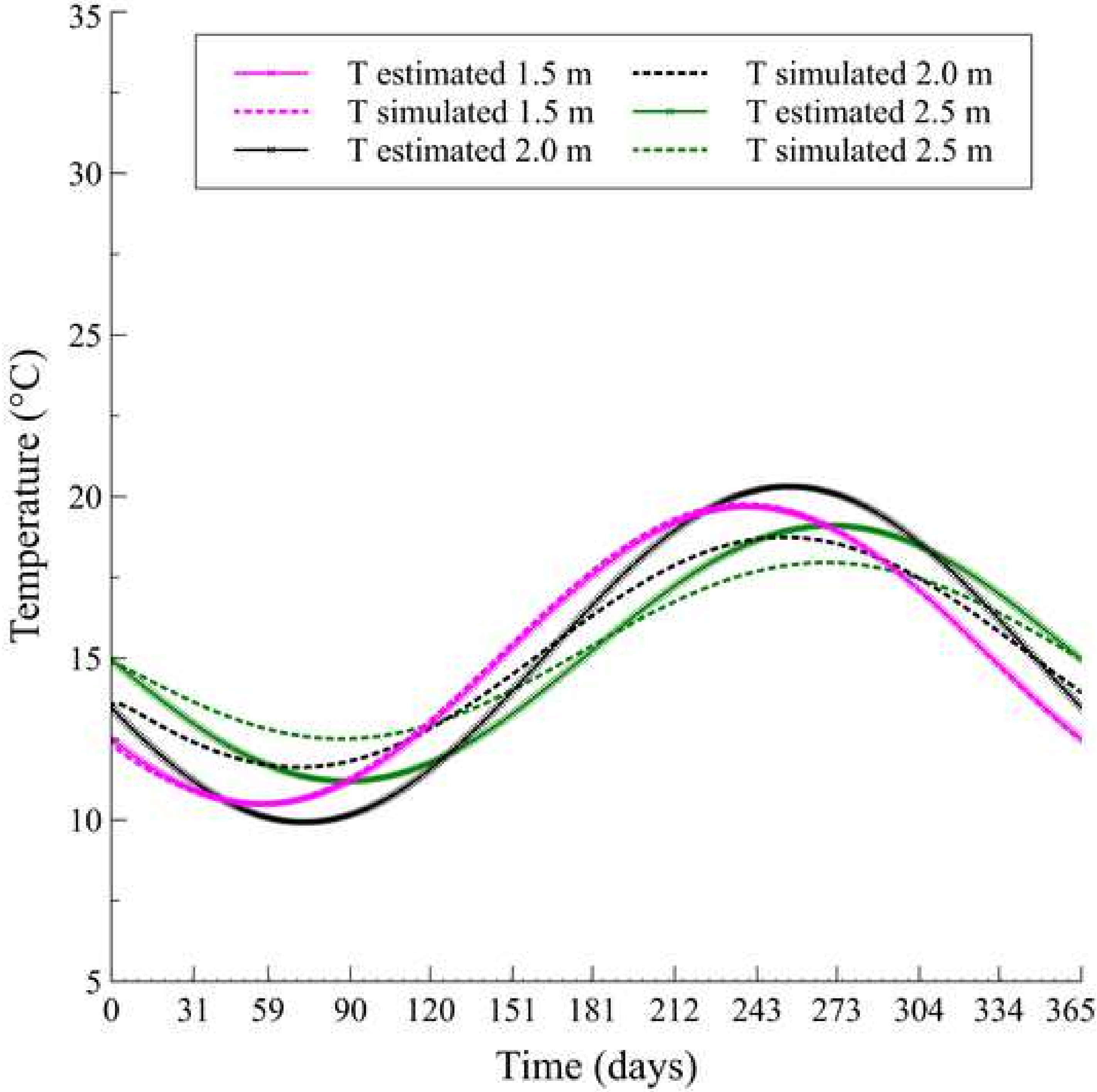

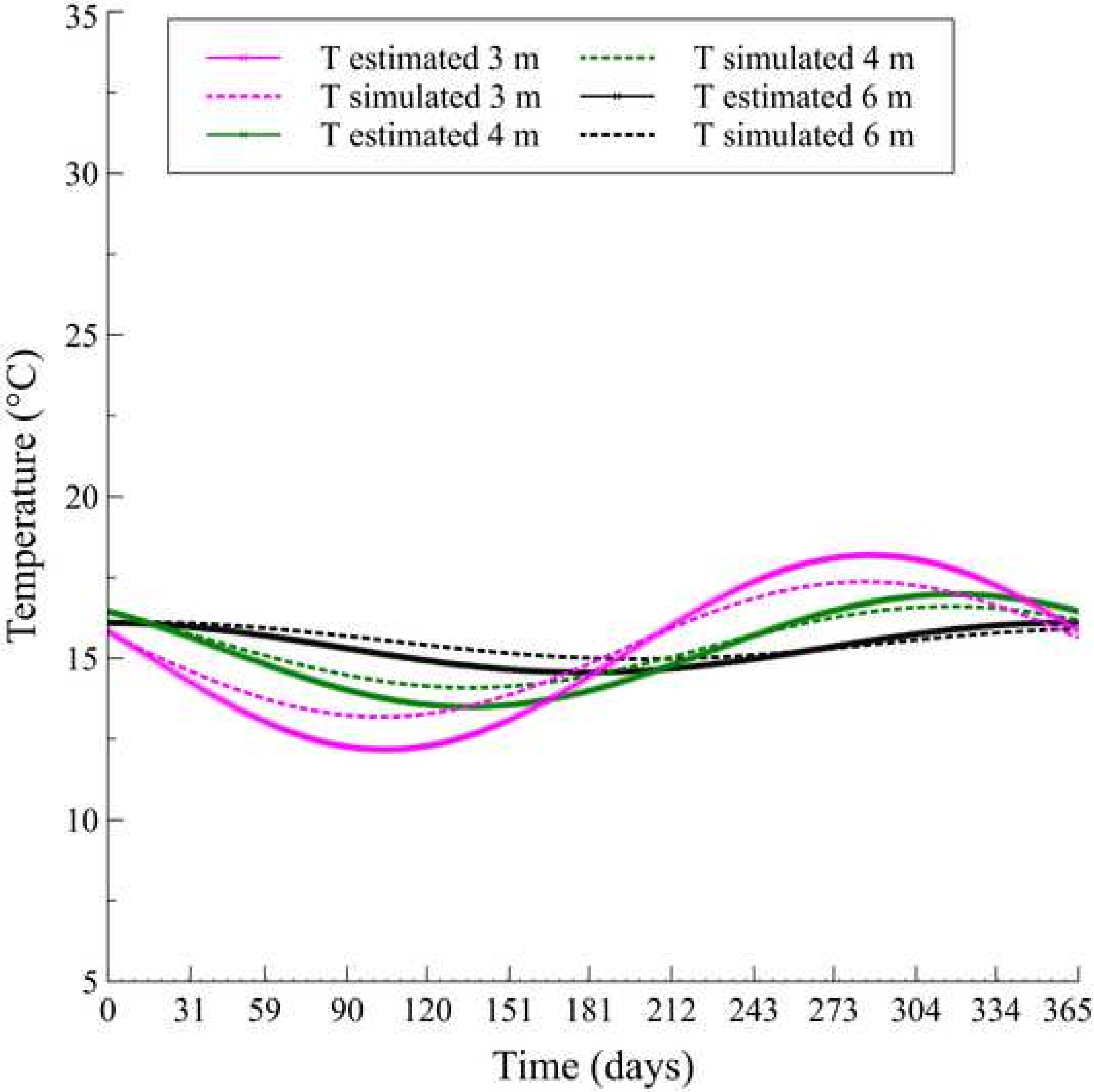
T estimated 3 m
T simulated 3 m
T estimated 4 m
T simulated 4 m
T estimated 6 m
T simulated 6 m
Temperature (°C)
35
30
25
20
15
10
5
0
31
59
90
120
151
181
212
243
273
304
334
365
Time (days)

5d

Click here to access/download;Figure;Figure5d.jpg

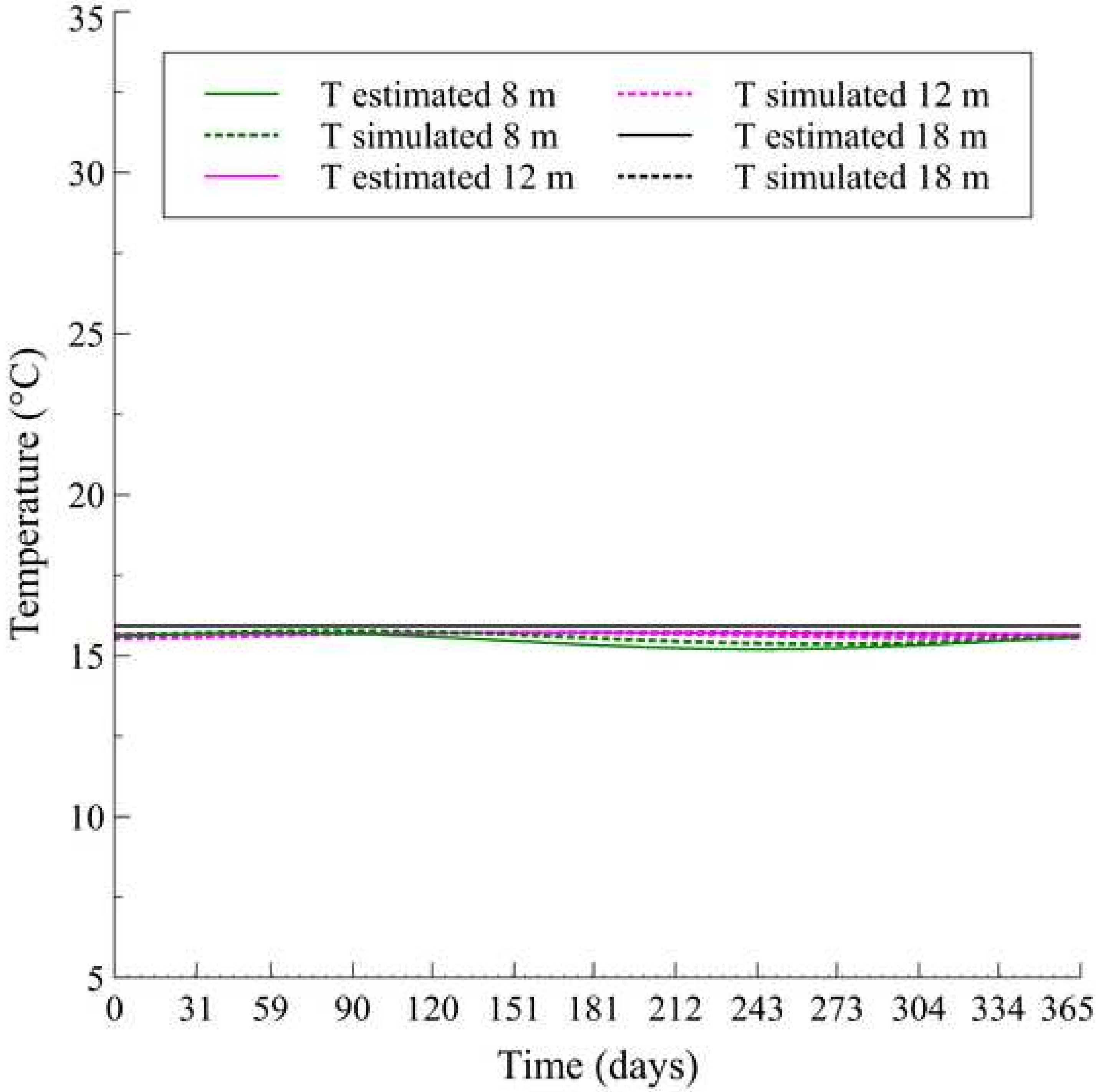

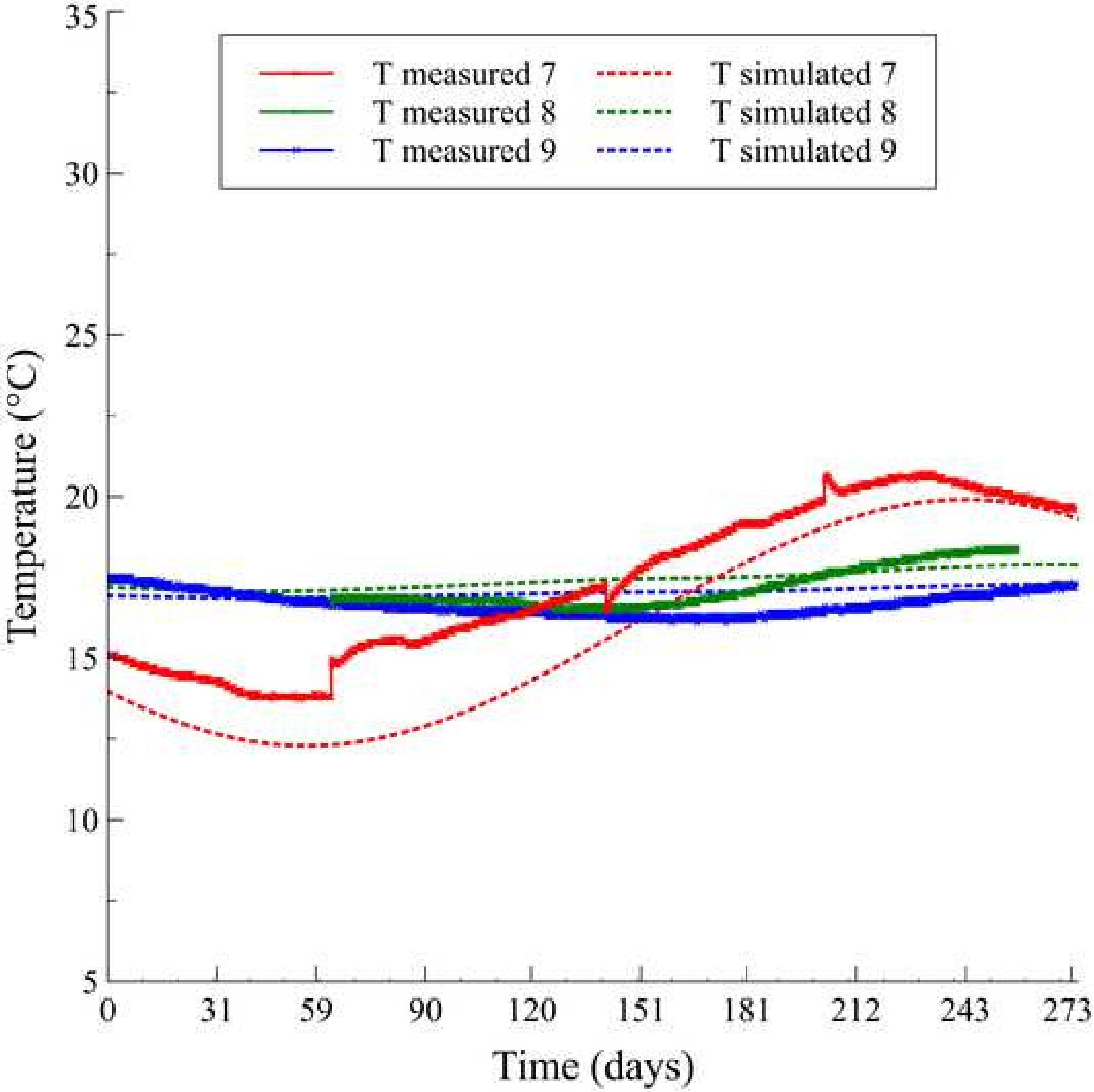

T measured 7
T measured 8
T measured 9
T simulated 7
T simulated 8
T simulated 9
Temperature (°C)
35
30
25
20
15
10
5
0
31
59
90
120
151
181
212
243
273
Time (days)

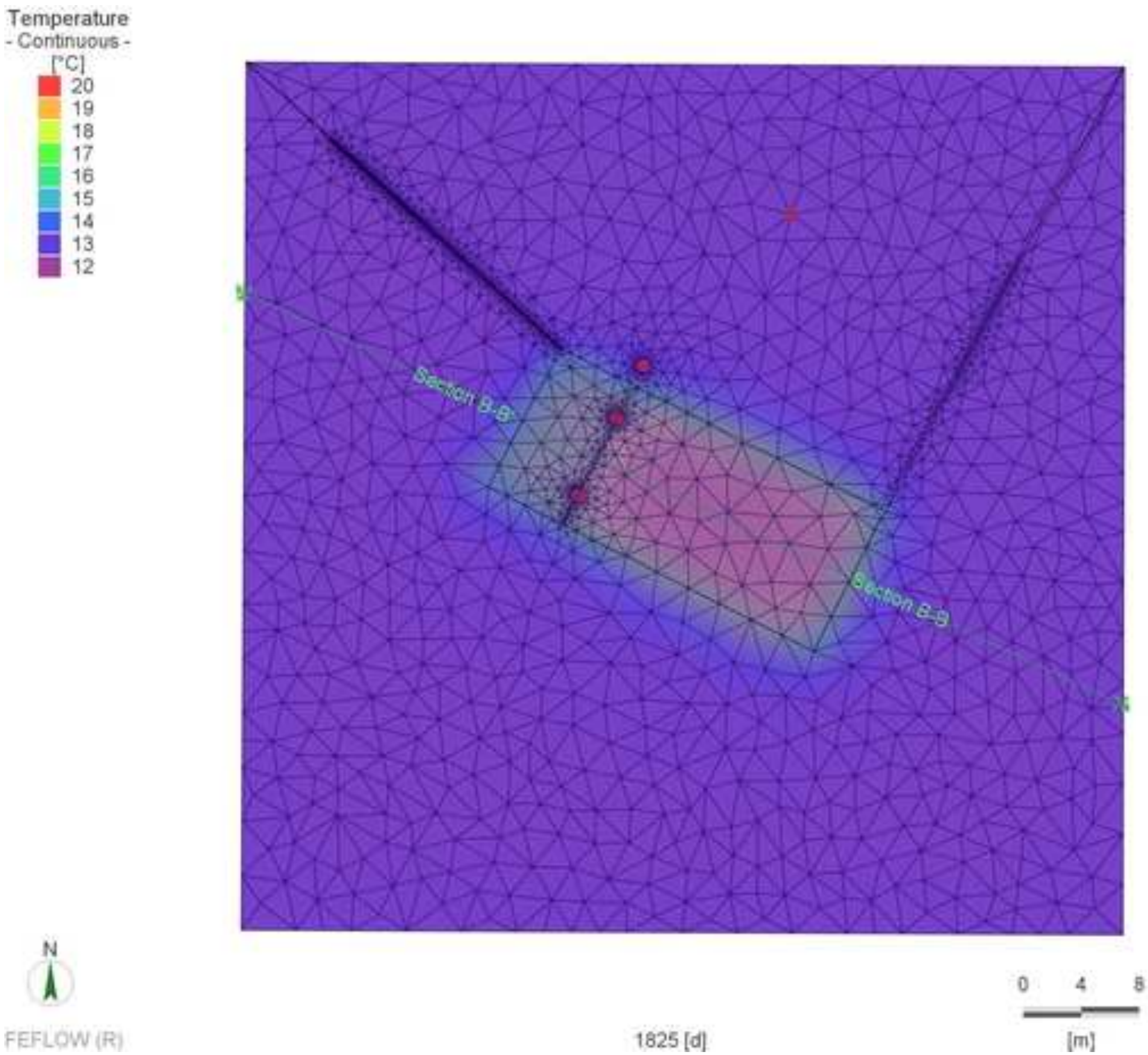

Temperature
- Continuous -
[°C]
20
19
18
17
16
15
14
13
12
Section B-B'
Section B-B'
N
FEFLOW (R)
1825 [d]
0
4
8
[m]

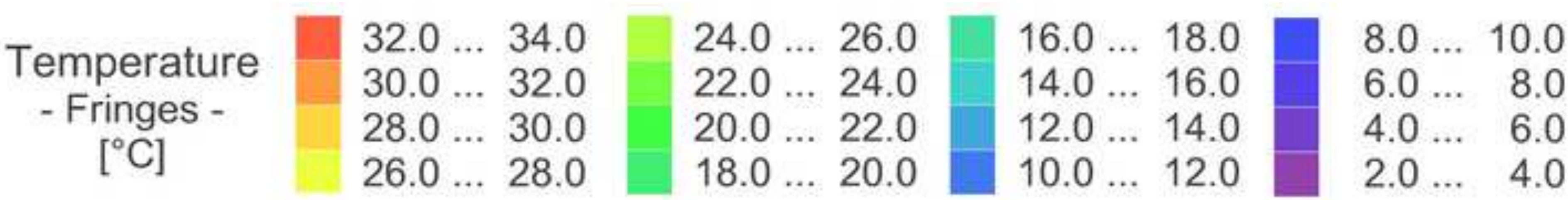
Temperature
- Fringes -
[°C]
32.0 ... 34.0
30.0 ... 32.0
28.0 ... 30.0
26.0 ... 28.0
24.0 ... 26.0
22.0 ... 24.0
20.0 ... 22.0
18.0 ... 20.0
16.0 ... 18.0
14.0 ... 16.0
12.0 ... 14.0
10.0 ... 12.0
8.0 ... 10.0
6.0 ... 8.0
4.0 ... 6.0
2.0 ... 4.0

8a1 Click here to access/download;Figure;Figure8a1.jpg

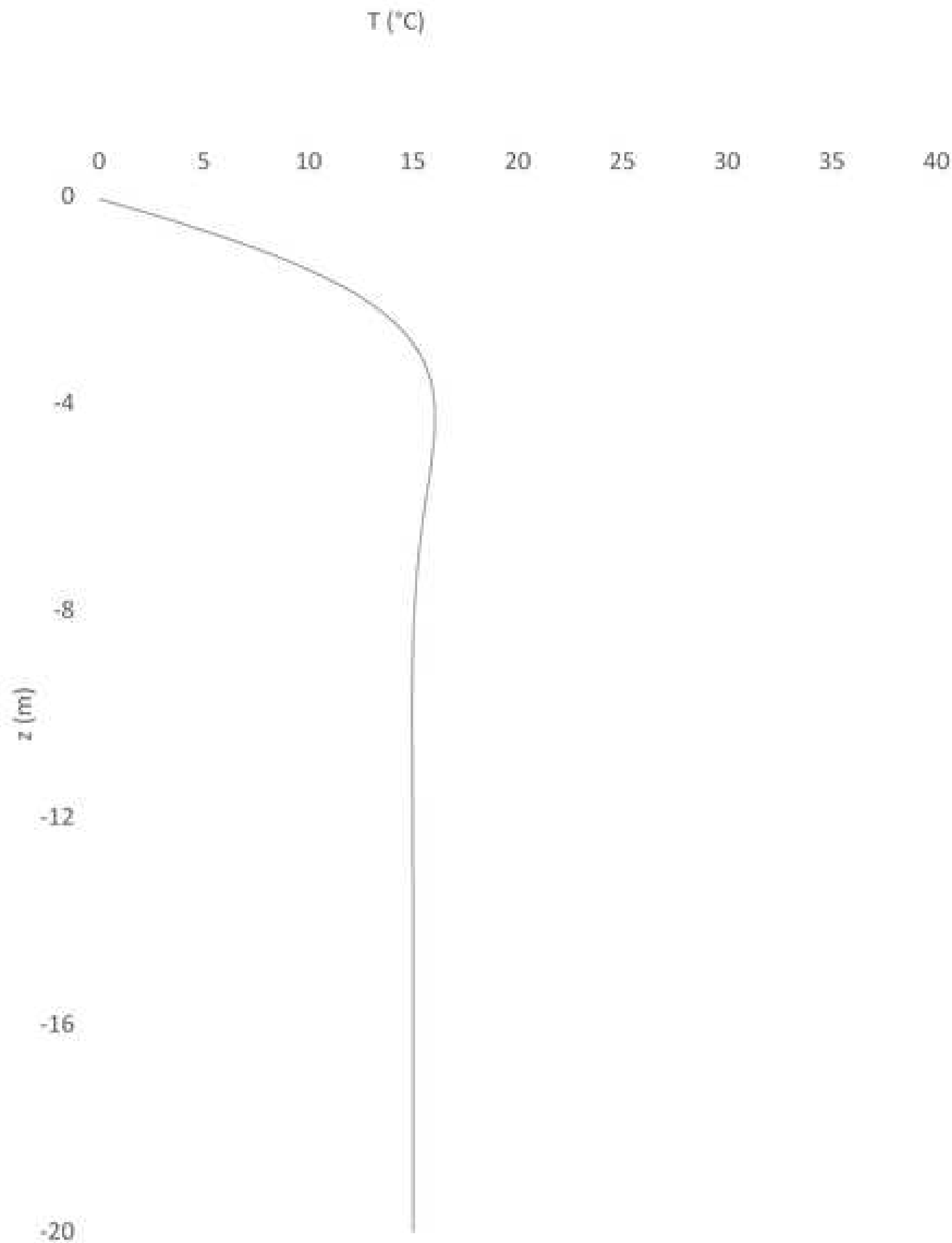

8a2

Click here to access/download;Figure;Figure8a2.jpg

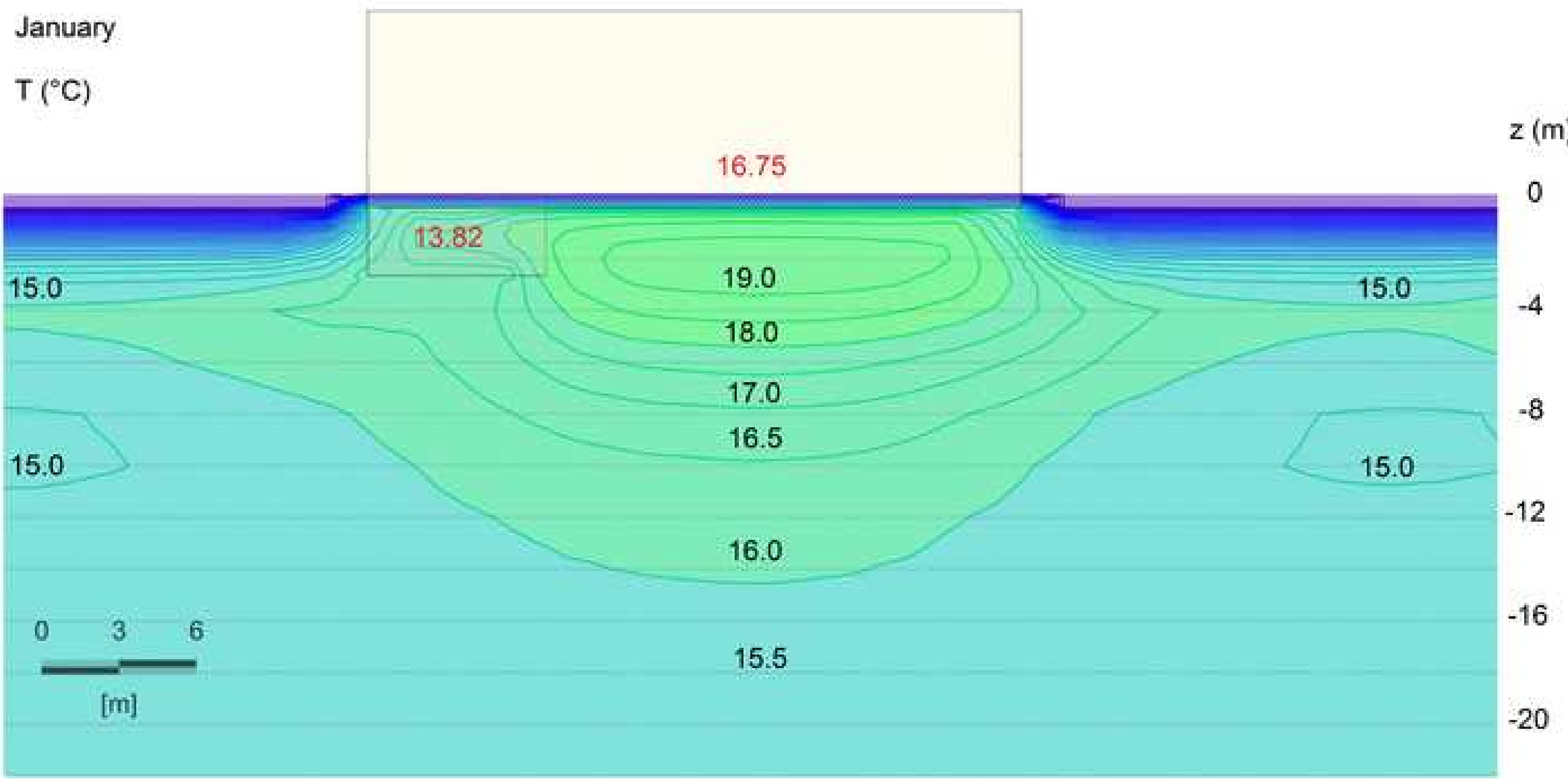

8b1 Click here to access/download;Figure;Figure8b1.jpg

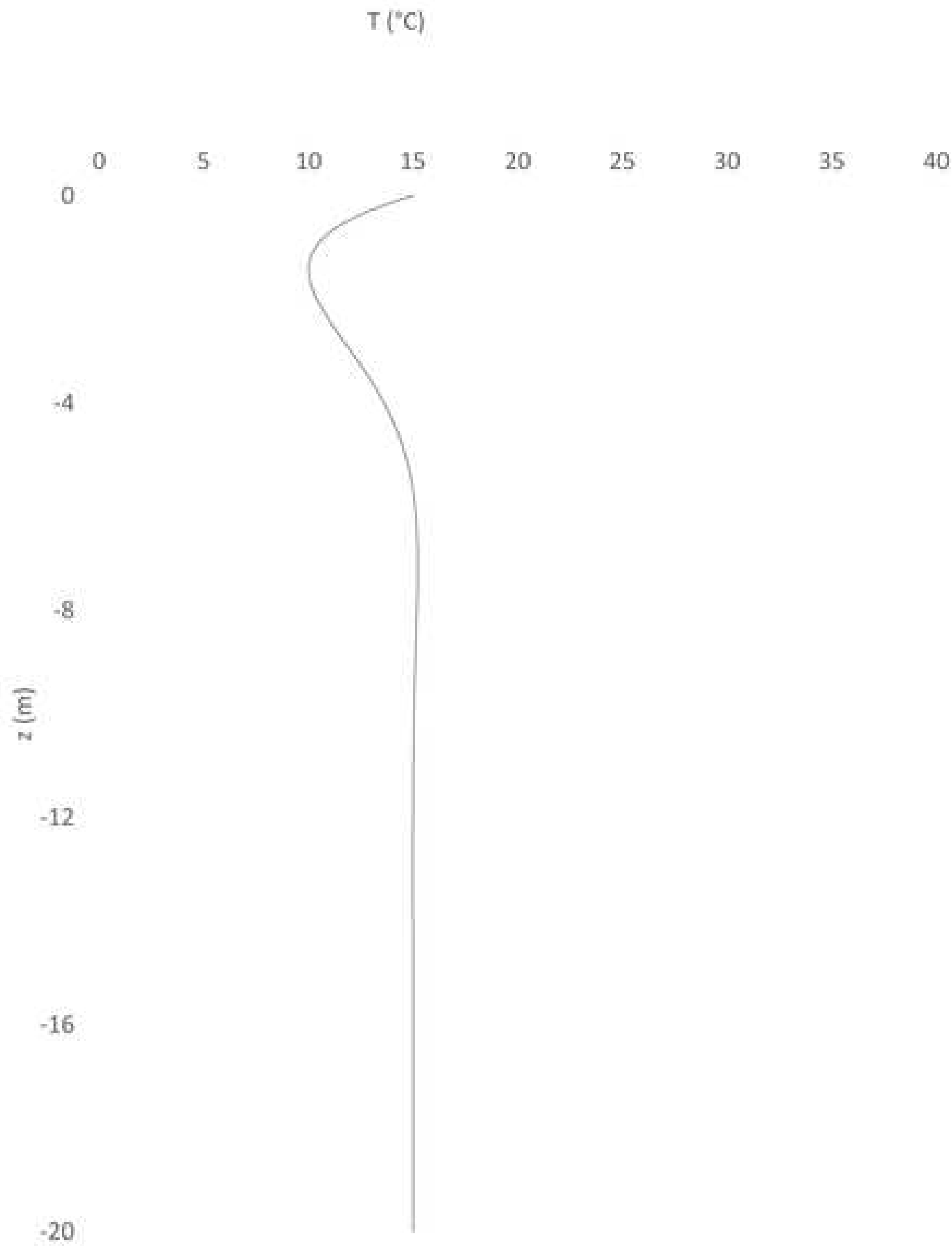

8b2 Click here to access/download;Figure;Figure8b2.jpg

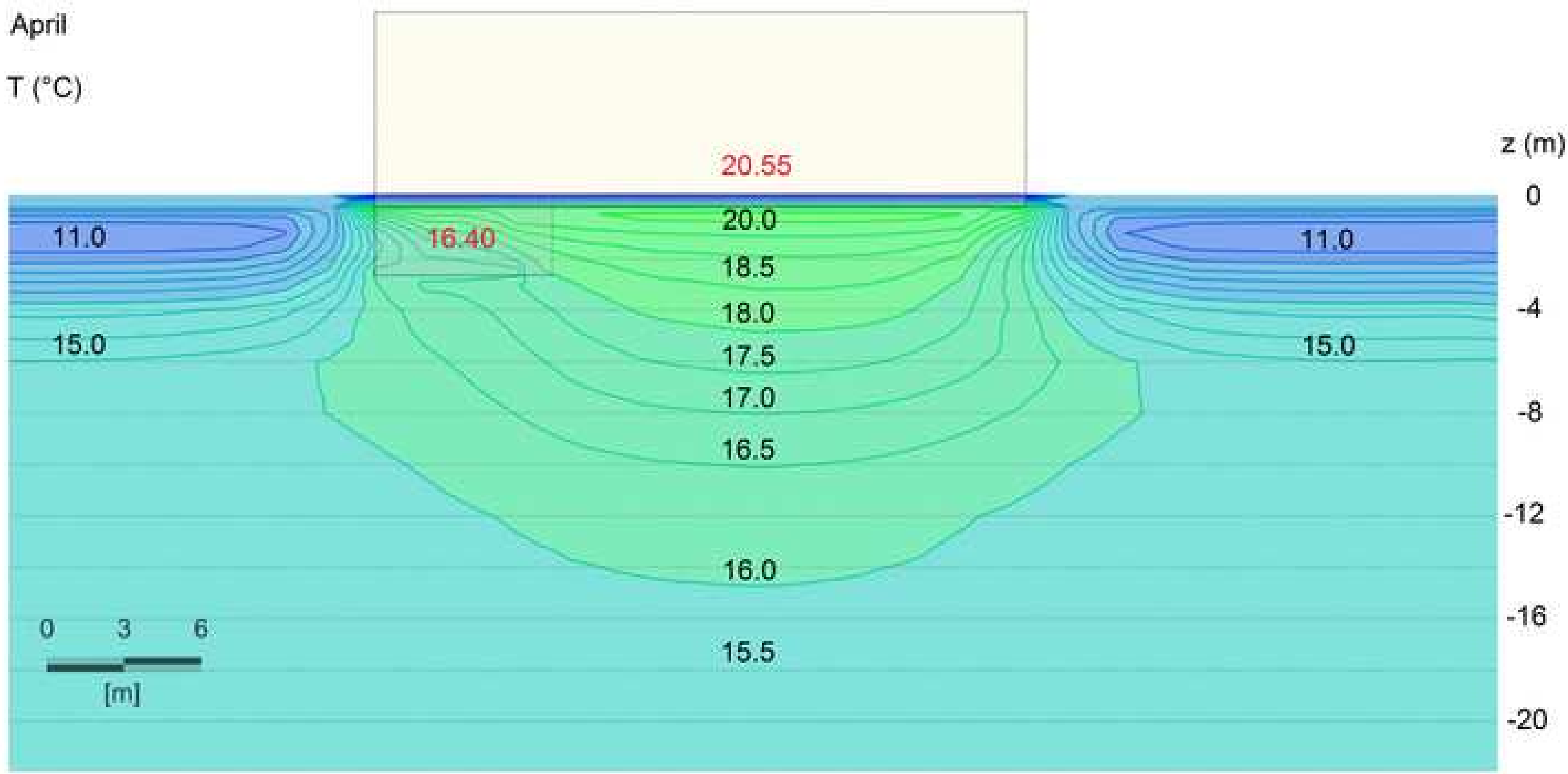

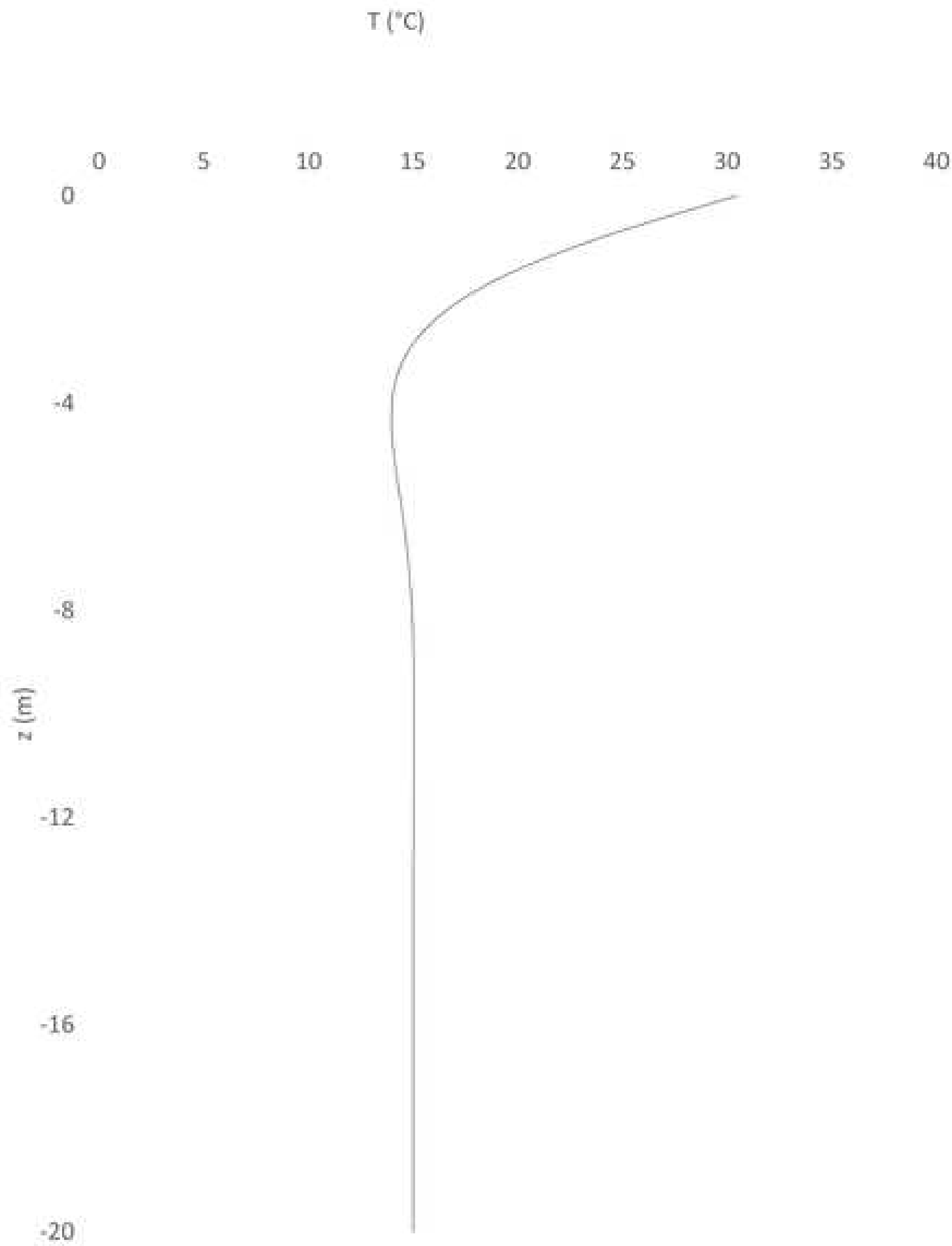
T (°C)
0
5
10
15
20
25
30
35
40
0
-4
-8
-12
-16
-20
z (m)

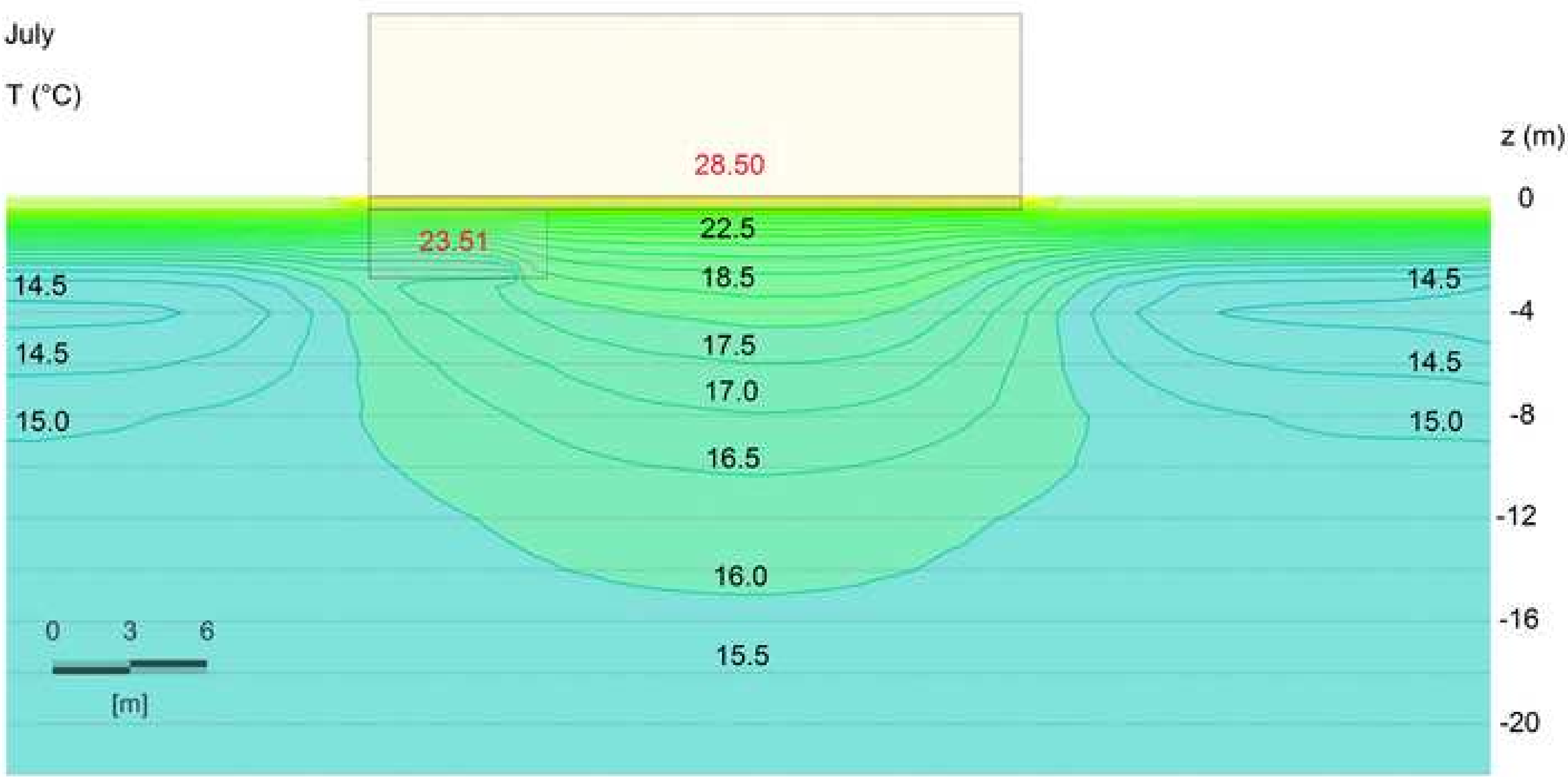
July
T (°C)
z (m)
28.50
0
23.51
22.5
18.5
14.5
14.5
-4
17.5
14.5
14.5
17.0
15.0
15.0
-8
16.5
-12
16.0
0 3 6
-16
15.5
[m]
-20

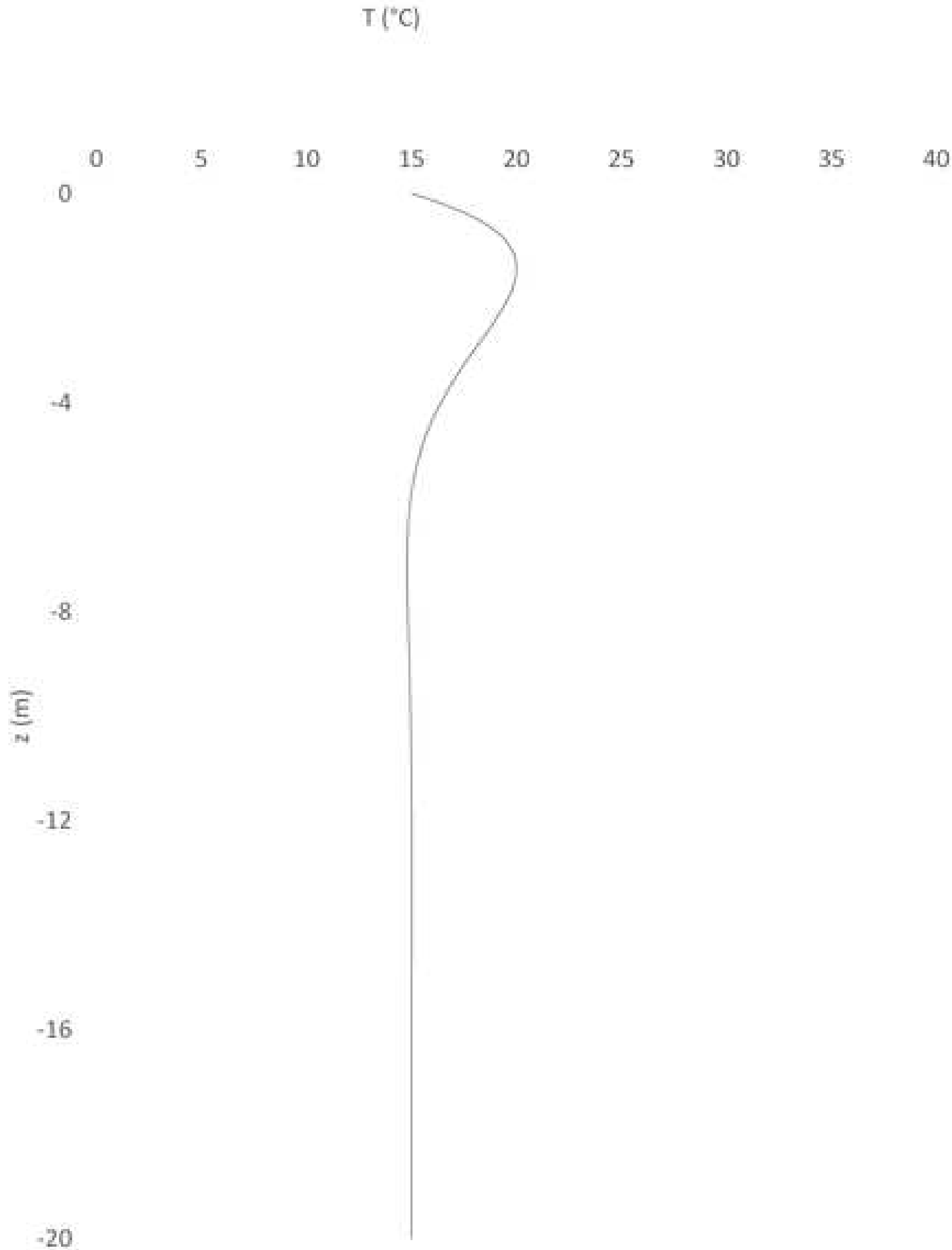
T (°C)
0
5
10
15
20
25
30
35
40
0
-4
-8
-12
-16
-20
z (m)

8d2

Click here to access/download;Figure;Figure8d2.jpg